LUND UNIVERSITY
Faculty of Science

Transport properties and full counting statistics of electrons in double quantum dots operated by Maxwell's demon

Björn Annby-Andersson

Thesis submitted for the degree of Master of Science
Project duration: 4 months (30 ECTS)

Supervised by Peter Samuelsson and Patrick Potts

Department of Physics
Division of Mathematical Physics
January 2019

Abstract

During recent years, Maxwell's demon has regained interest in the work of understanding the connection between thermodynamics and information theory. This thesis presents transport properties of electrons in a double quantum dot system operated by Maxwell's demon. The demon transports electrons from a lower to higher chemical potential through a pump-like scheme without performing any net work on the electrons. To describe and simulate the dynamics of the system, we use rate equations, full counting statistics, and a Monte Carlo method. We observe that the implementation of the demon works, and that the three approaches give the same results.

Acknowledgements

I would like to thank my supervisors Peter Samuelsson and Patrick Potts for their splendid supervision and guidance during this project.

Abbreviations and acronyms

QD	quantum dot
QDL	left quantum dot
QDR	right quantum dot
FCS	full counting statistics

Contents

Chapter 1

Introduction

During the last decade, thermodynamics has gained new interest among scientists from several research disciplines due to an improvement in experimental control of quantum systems. The aim is to extend thermodynamics and non-equilibrium statistical physics into *quantum thermodynamics*, a theory of thermodynamics including quantum effects and ensemble sizes well below the thermodynamic limit [1]. As the size of technological components is decreasing towards the nanoscale, quantum thermodynamics is believed to play an important role in the industry, and as the field is developing, new technologies, utilizing quantum thermodynamic properties, may be discovered [1].

Promising candidates for studying quantum thermodynamics are electronic circuits operating at sub-Kelvin temperatures [2]. The temperatures of these systems can be measured locally with precision, and they offer large statistical samples for experiments [2]. Circuits equipped with nano-components, such as quantum dots, single electron boxes and superconducting qubits, form basic units for studying heat transport, entropy production and work [2].

A famous paradox in thermodynamics is Maxwell's demon, a creature that appears to violate the second law of thermodynamics in non-equilibrium processes. In 1961, Rolf Landauer formulated the Laudauer erasure principle [3] that was used to solve the paradox; the demon uses information and converts it to energy in the form of useful work [4]. During recent years, Maxwell's demon has gained lots of interest among scientists; it has been sudied both theoretically and experimentally [5]-[9]. In experiments, the demon can be realized as a detector gathering information about a system by measuring its state. The information can then be used in a feedback loop to manipulate the system to produce an output power. At the moment, the output effects are tiny, but are believed to be enhanced with the help of feedback [2]. Further implementations of Mazwell's demon are of interest since they can contribute to the understanding of information-to-energy conversion and how feedback can be used to increase the output effects.

This thesis investigates the transport properties and full counting statistics of electrons in two coupled single level quantum dots that are operated by a Maxwell demon. Transport properties, as current and current fluctuations, have been of great interest as these properties have proven to be of importance in the understanding of mesoscopic systems [10]. For example, shot noise measurements played important roles in the observation of the fractional charge of quasi-particles [11]-[14]. We show that the implementation of the demon works in theory by using three approaches. First, rate equations give basic information about the electron transport, such as current and electrical power. Secondly, full counting statistics gives the complete information about the transport properties

through a probability distribution describing the number of electrons transferred through the system within a given time; this study is performed both analytically, and numerically, and involves the cumulants of the probability distribution that are closely related to current and current fluctuations. Finally, the analytics and numerics are compared with a Monte Carlo simulation of the demon. We observe that the three approaches give the same results. Furthermore, the study acts as a starting point for further research on the system that can contribute to the understanding of information-to-energy conversion in nano-sized systems.

The thesis is divided into four parts. Chapter 2 presents the double quantum dot system, the theoretical tools that were used, and how they were applied. In chapter 3, the results are presented and discussed, and chapter 4 and 5 are devoted to conclusions and outlook.

Chapter 2

Double quantum dot system and theoretical tools

This chapter introduces the double quantum dot (QD) system that is studied in this thesis. The general features of the system are described in Sec. 2.1, and the succeeding sections introduce theoretical concepts and how they are applied to the system. These concepts are: Maxwell's demon in Sec. 2.2; rate equations for open systems in Sec. 2.3; full counting statistics in Sec. 2.4; and finally, the methodology for a Monte Carlo simulation of the double QD system is presented in Sec. 2.5.

2.1 The double quantum dot system

The system studied in this work is composed of two tunnel-coupled single level quantum dots (QD). The QDs are, in their turn, in contact with one electron reservoir each; the complete setup is displayed in Fig. 2.1. The reservoirs and the QDs will be referred to as left or right, and the properties of the complete system will be marked with L or R to distinguish whether they belong to the left- or the right-hand side. Electrons in the left reservoir can tunnel into the left QD (QDL), and the tunneling rate for this process is given by Γ_L. The tunneling rate for electrons going from the left to the right QD (QDR) is given by γ, and finally, the tunneling rate for electrons going from the right QD to the right reservoir is given by Γ_R.

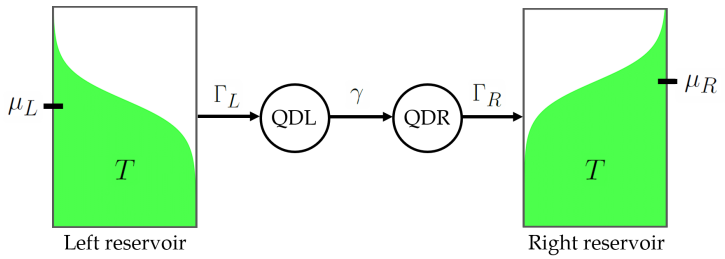

Figure 2.1: *A sketch of the system studied in this thesis. Two quantum dots, QDL and QDR, are coupled in series. The dots are in contact with one electron reservoir each. The reservoirs have the same temperature T, but different chemical potentials, μ_L and μ_R, respectively. Electrons can tunnel between the system constituents, and this occurs with tunneling rates Γ_L, γ and Γ_R.*

The reservoirs are assumed to be in equilibrium, and have well defined temperatures,

T_L and T_R, and chemical potentials, μ_L and μ_R. Throughout this thesis, the two reservoirs will have the same temperature $T = T_L = T_R$, but different chemical potentials, $\mu_L \neq \mu_R$. The average electron occupation numbers of the reservoirs are hence described by the Fermi distributions $f_L(\epsilon_L)$ and $f_R(\epsilon_R)$, respectively. These distributions are given by

$$f_{L(R)}(\epsilon_{L(R)}) = \left(e^{(\epsilon_{L(R)} - \mu_{L(R)})/k_B T} + 1\right)^{-1} \tag{2.1}$$

where k_B is the Boltzmann constant.

The QDs sketched in Fig. 2.1 can, for instance, be realized in InAs/InP nanowire heterostructures [15], or by growing wurtzite segments in zinc blende InAs nanowires [16]. A simplified depiction of a InAs/InP nanowire is displayed in Fig. 2.2. As can be seen in the figure, the QDs are confined in the regions between InAs and InP. In addition, two gates are in contact with the QDs, and the gate voltages V_L and V_R can control the potential profiles of the dots.

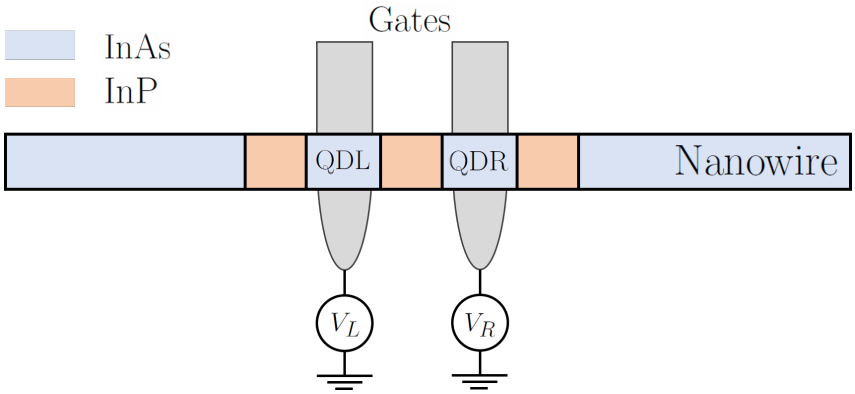

Figure 2.2: *The figure shows how the QDs can be fabricated in a nanowire. The regions confined in between InAs and InP constitute the QDs. The gates can control the potential profiles of the QDs by tuning the gate voltages V_L and V_R.*

The QDs have one energy level each, ϵ_L and ϵ_R, which can be moved between three positions by the tuning the gate voltages V_L and V_R. There is one lower position with energy ϵ_l, one middle position with energy ϵ_0 and one upper position with energy ϵ_u, see Fig. 2.3. Here, it is assumed that at most one electron can occupy each energy level, and this is achieved by having an infinitely large intra-dot Coulomb repulsion.

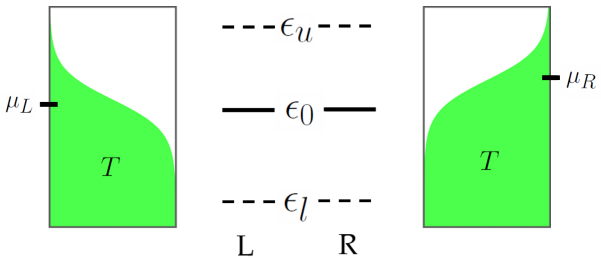

Figure 2.3: *Illustration of the QD's tunable energy levels and the Fermi distributions of the electron reservoirs. The left and right boxes are the electron reservoirs, and the green regions represent their Fermi distributions. In between the reservoirs, the energy levels of the left (L) and right (R) QDs are sketched, and their positions are marked with solid or dashed lines. The energy levels can be moved between the three positions by tuning the gate voltages V_L and V_R (see Fig. 2.2).*

It is also assumed that the Coulomb repulsion energy, U, between the two dots is so large that only one of the dots can be occupied at a time. This can be achieved by choosing U such that $(\epsilon_i + U - \mu_{L/R}) \gg k_B T$, $i = l, 0, u$. It will also be assumed that ϵ_u and ϵ_l are chosen such that $(\epsilon_u - \mu_{L/R}) \gg k_B T$ and $(\epsilon_l - \mu_{L/R}) \ll k_B T$. In this way, we can in practice set $f_{L/R}(\epsilon_u) = 0$ and $f_{L/R}(\epsilon_l) = 1$.

In addition, it is assumed that all the couplings in the system are weak. In particular, the coupling between the QDs is assumed to be sufficiently weak such that environmental noise suppresses any coherence between the dots. Hence, the system can be in one of three states: empty, $|00\rangle$, or occupied by one electron either in the left QD, $|10\rangle$, or in the right QD, $|01\rangle$. Since coherence will not be present, the dynamics of the system can be described by a classical rate equation; this will be further discussed in Sec. 2.3.

2.2 Maxwell's demon

This section discusses the paradox called Maxwell's demon, and how it can be solved by using Landauer's erasure principle. In particular, Sec. 2.2.1 explains how Maxwell's demon is implemented in the double quantum dot system.

General description of Maxwell's demon

Maxwell's demon is a paradox introduced by James Clerk Maxwell in 1871 where he, in a letter [17], presented a thought experiment that seems to violate the second law of thermodynamics. The thought experiment involves a gas-filled chamber which is divided into two compartments by a wall with a door, see stage 1 in Fig. 2.4. The two compartments are completely isolated when the door is closed.

Initially, the door is open so that the gas in the entire chamber can reach thermal equilibrium, that is, when the temperature, T, of the gas is uniform throughout the chamber. The average speed of the particles at this temperature is given by $\langle v \rangle_T$. A particle which has a speed greater than $\langle v \rangle_T$ is said to be fast, while a particle with a speed smaller than $\langle v \rangle_T$ is slow.

Imagine a demon that can operate the door without exerting any work on it. In addition, the demon can see individual particles, and determine their speed. If a fast particle approaches the door from the left, the demon can open the door and allow the particle to enter the right compartment. If instead a slow particle approaches the door from the right, the demon can open the door, allowing passage for the slow particle into the left compartment. In this manner, the demon can separate all the fast and slow particles such that the two compartments reach new thermal equilibriums with different temperatures, T_L and T_R, respectively, where $T_L < T_R$. After this separation process, the system is in stage 2 in Fig. 2.4.

At stage 3 in Fig. 2.4, a heat engine is connected to the two compartments, and by making use of their temperature difference, the work W can be extracted. In the fourth stage, a heat bath brings the temperature of the compartments back to the initial temperature T. In the end, it appears as if work has been extracted from a single heat bath, something that violates the Kelvin-Planck statement of the second law.

It is, furthermore, well-known that the process going from stage 2 to 1, in Fig. 2.4, is allowed by the second law since the change of entropy $\Delta S_{2\to1} \geq 0$. As a consequence, it is not allowed to go from stage 1 to 2 since $\Delta S_{1\to2} < 0$. One could, in other words, argue that stage 2 is much more ordered than stage 1. The system, therefore, strives to

be in stage 1 to maximize the entropy. Hence, it appears that the demon is violating the second law when separating slow and fast particles.

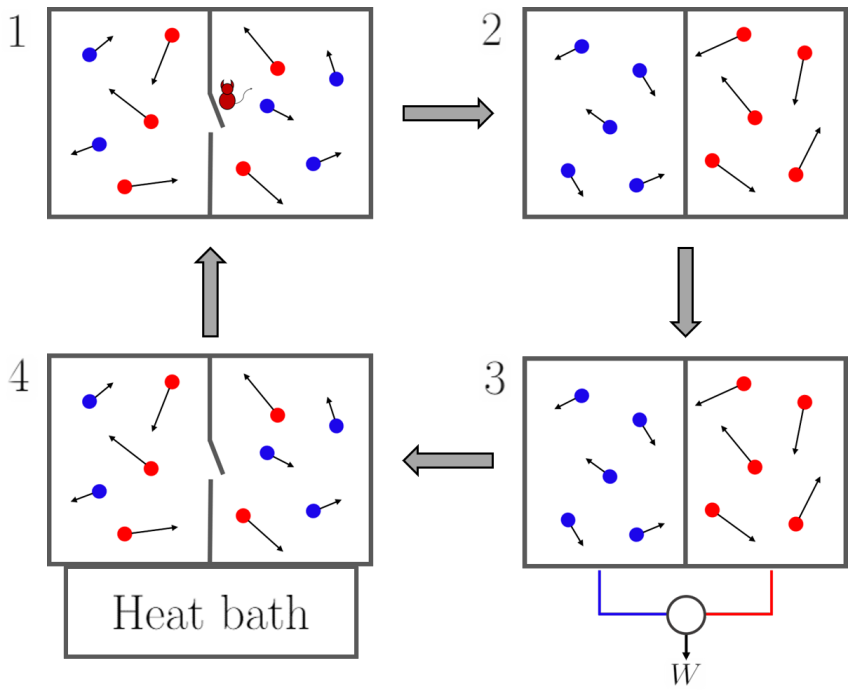

Figure 2.4: *A cyclic process extracting work from a single heat bath. The cycle starts in (1) with a gas-filled chamber which is in thermal equilibrium and has temperature T. A demon can separate slow (blue) and fast (red) particles by using the door between the compartments. In (2), the slow and fast particles have been separated by the demon, and the compartments end up having different temperatures. In (3), a heat engine utilizes the temperature difference by converting heat to useful work. In (4), the door is open such that particles from the different compartments can mix. In addition, a heat bath is connected to the chamber to bring the gas back to the initial temperature and the cycle is completed.*

This demon can be referred to as a *temperature demon*. Other types of Maxwell's demon are also possible; in [18], a *pressure demon* is described for example, and as we will see in Sec. 2.2.1, a demon can be used to transport electrons against a voltage bias. The latter type of demon has been realized experimentally in [7] and [**?**].

Landauer's erasure principle as a solution to Maxwell's demon

To understand why Maxwell's demon does not violate the second law, one has to consider the demon as a physical system itself. Therefore, the entropy production in the combined unit, i.e. system + demon, must satisfy the second law. This means that the entropy can be decreased in the system as long as the entropy production in the demon balances the decrease such that the second law is fulfilled.

The process visualized in Fig. 2.4 appears impossible to construct physically, but the paradoxical situation can be circumvented by considering Landauer's erasure principle [3, 4]. Landauer's erasure principle states that the erasure of 1 bit of information requires a minimum dissipation of heat, $Q_{erase}^{min} = k_B T \ln(2)$, which is dissipated to a surrounding environment in equilibrium that has the temperature T [1]. If the first stage of the cycle in Fig. 2.4 is considered once again, it is assumed that the demon has a memory which

initially is blank. When the demon separates the slow and fast particles, it first acquires information about which type of particles that is approaching the door, and then stores that information in its memory. To completely return to the initial state after one cycle, the demon has to erase its memory. When erasing the memory, the demon dissipates the heat $Q_{erase} \geq W$ into the system [3, 4], and hence, the process is thermodynamically allowed, and is not breaking the second law; this should be the case when treating the memory as a thermodynamic system.

2.2.1 Maxwell's demon in the double QD system

By operating the double QD system in the spirit of Maxwell's demon, electrons can be transported from a lower to a higher chemical potential without exerting any net work on the electrons. This is something that is seemingly forbidden by the second law of thermodynamics. The electron reservoirs in the double QD system can exchange electrons with each other, and the change of entropy in the reservoirs caused by electrons leaving or entering the reservoirs is given by

$$\Delta S_{L/R} = \frac{\epsilon_0 - \mu_{L/R}}{T} \Delta n_{L/R}, \tag{2.2}$$

where T is the temperature of the reservoirs, $\Delta n_{L/R}$ is the change of number of electrons in the left/right reservoir, and ϵ_0 is the energy of the electrons when they leave or enter the reservoirs. In this thesis, all electrons leave and enter the reservoirs with energy ϵ_0. Equation (2.2) is Clausius inequality $\Delta S \geq Q/T$ with an equal sign which tells us that the process of electrons leaving and entering the reservoirs is reversible. We can assume the process to be reversible if we consider the reservoirs to be infinitely large. Then the temperature changes in the reservoirs, due to electrons leaving and entering, are so small that the temperature of the reservoirs in practice is constant. Therefore, we consider the process to be quasi-static because the reservoirs never are driven out from equilibrium, and reversibility is possible. The chemical potentials, μ_L and μ_R, are assumed to obey $\mu_L < \mu_R$ and it is further assumed that the number of electrons in the system is constant, i.e. $\Delta n_L = -\Delta n_R$. The total entropy change in the reservoirs is then given by

$$\Delta S = \Delta S_L + \Delta S_R = \frac{\Delta n_R}{T}(\mu_L - \mu_R), \tag{2.3}$$

and Δn_R must hence be negative to fulfill the second law. In conclusion, the second law tells us that the electrons move towards the lower chemical potential if no net work is exerted on the electrons.

A demon can, however, circumvent the second law, if the entropy production of the demon is not taken into account, by operating according to the following scheme where it is assumed that the demon can measure the electron occupation of the QDs perfectly:

1. Initially, the system is empty ($|00\rangle$), with the energy levels positioned at $\epsilon_L = \epsilon_0$, and $\epsilon_R = \epsilon_u$. With this positioning, electrons can tunnel from the left reservoir to the left QD, but electrons in the right reservoir cannot tunnel to the right QD.

2. When an electron tunnels from the left reservoir to the left QD, the system transits to the state $|10\rangle$, and the left and right energy levels are instantaneously moved by the demon to the lower position, $\epsilon_L = \epsilon_R = \epsilon_l$. From here, the only transit possible is the one to $|01\rangle$, because of Coulomb repulsion.

3. When the system transits to $|01\rangle$, the demon moves the energy levels instantaneously to $\epsilon_L = \epsilon_u$, and $\epsilon_R = \epsilon_0$. When the electron tunnels into the right reservoir, the system returns to $|00\rangle$, and the cycle can start over in step 1.

A visualization of the process is displayed in Fig. 2.5.

In this thesis, we define work to be useful if $W > 0$, and heat to be released from the reservoirs if $Q < 0$. Similarly, if $Q > 0$, heat is considered to enter the reservoirs. It should also be noted that we, in this thesis, mostly consider the case where $\mu_L < \epsilon_0 < \mu_R$, but this inequality is, as we will see, not a necessary condition for the demon to work. For each electron that is transferred from the left to the right reservoir according to the scheme above, heat from the reservoirs is converted into useful work. When an electron leaves the left reservoir, and tunnels to the left QD, the heat $Q_L = -(\epsilon_0 - \mu_L)$ is released from the left reservoir. Similarly, when an electron tunnels to the right reservoir, the heat $Q_R = (\epsilon_0 - \mu_R)$ is released from the right reservoir. The total heat released is given by $Q_{tot} = Q_L + Q_R = eV$ if the voltage bias V across the reservoirs is $\mu_L - \mu_R = eV$. Here, e is the elementary charge, and it is considered to be a positive quantity throughout the thesis.

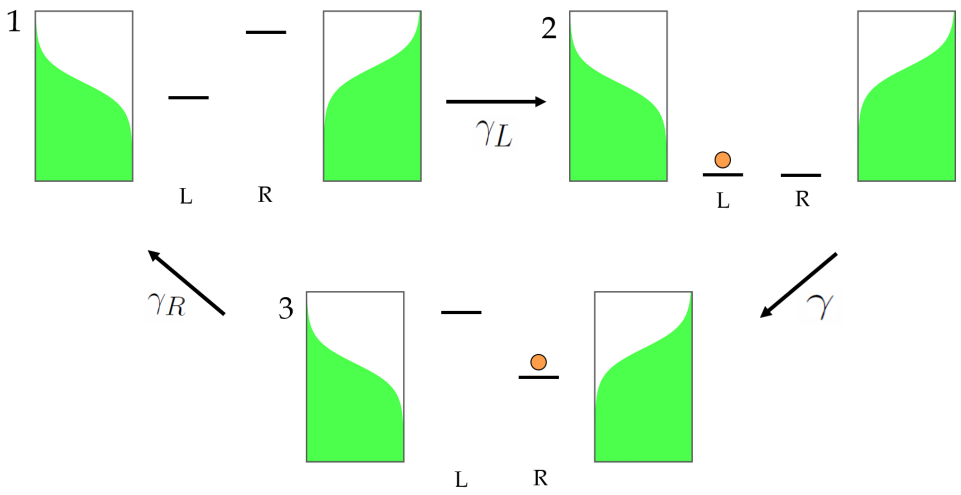

Figure 2.5: *(1) Initially, the double QD system is in the state* $|00\rangle$*. (2) When an electron tunnels into the left QD, the system transits to the state* $|10\rangle$*, and the energy levels are moved to* ϵ_l*. (3) As the electron tunnels to the right QD, and the* $|01\rangle$*-state becomes occupied, the energy levels are moved up. When the electron tunnels to the right reservoir, the system starts over at step 1.*

When m electrons have been transferred to the right reservoir, the total heat is $Q_{tot}^{(m)} = meV$, and since the complete system does not exchange energy with its surroundings, the first law of thermodynamics implies that the heat is converted into useful work. Thus, with m electrons being transferred to the right reservoir, the total work is $W_{tot}^{(m)} = -Q_{tot}^{(m)} = -meV$. For $V < 0$, or in other words, when the right chemical potential is higher than the left, $W_{tot}^{(m)} > 0$.

The demon can measure the occupation of the QDs by using a device that is sensitive to electric charge; examples of such devices are single electron transistors or quantum point contacts. Between step 1 and 2 in the scheme described above, the demon measures that the left QD is occupied, and by tuning the gate voltages (see Fig. 2.2), the energy levels can be moved. As the left energy level is moved, the work $-(\epsilon_0 - \epsilon_l)$ is performed

on the electron by the left gate. Similarly, when the right energy level is moved between step 2 and 3, the right gate performs the work $(\epsilon_0 - \epsilon_l)$ on the electron. Consequently, the total work performed by the gates to transport one electron is

$$W_g = -(\epsilon_0 - \epsilon_l) + (\epsilon_0 - \epsilon_l) = 0. \tag{2.4}$$

In the end, we see electrons being transferred from a lower to higher chemical potential without any net work acting on them.

2.3 Rate equation for open systems

The first part of this section presents how rate equations can be used to describe the dynamics of open systems without coherences. In Sec. 2.3.1, the rate equation for the double QD system is introduced.

A system, S, which can exchange both energy and matter with its surroundings is considered to be an open system. A typical surrounding is some energy or particle reservoir which is coupled to the system.

Here, S is assumed to be tunnel-coupled to two particle reservoirs that can exchange particles and energy with S. It is further assumed that S has N discrete states. Particle interactions can be present in S, and electron-electron interaction is one possible example. These interactions play an important role when the transport properties of the composite system (S + reservoirs) are studied since they determine the trajectories of the particles. Moreover, the reservoirs are assumed to be in equilibrium, and has well defined temperatures, T_1 and T_2, and chemical potentials, μ_1 and μ_2. It is further assumed that no particle interactions are present, and therefore, the reservoirs are described by distribution functions whose properties are determined by the particle type, i.e. boson or fermion. The Hamiltonian of the composite system can be written as

$$\hat{H} = \hat{H}_S + \hat{H}_{B1} + \hat{H}_{B2} + \hat{H}_I \tag{2.5}$$

where $\hat{H}_S$ is the Hamiltonian for S, $\hat{H}_{B1}$ and $\hat{H}_{B2}$ are the Hamiltonians for the reservoirs and $\hat{H}_I$ is the Hamiltonian describing the coupling between S and the reservoirs.

In the weak tunneling regime, the coupling Hamiltonian, $\hat{H}_I$, can be considered as a weak perturbation, and hence, the transition rates for tunneling into different states in S are given by Fermi's golden rule. It is assumed that environmental noise decoheres the system, and when no coherence is present, the probability for a state k in S to be occupied is given by $P_k(t)$ and satisfies [19]

$$\frac{d}{dt}P_k(t) = \quad - \sum_{l=1,l\neq k}^{N} M_{lk}P_k(t) \quad + \sum_{l=1,l\neq k}^{N} M_{kl}P_l(t). \tag{2.6}$$

Here, M_{kl} is the transition rate for the transition going from state l to k. The first term on the right hand side of Eq. (2.6) can be understood as the rate for leaving the state k, provided that the system is in state k, and similarly, the second term is the rate for entering the state k given that S was in some state $l \neq k$.

Since there are N states in S, Eq. (2.6) gives N coupled differential equations which can be written in a more compact way as,

$$\frac{d}{dt}\boldsymbol{P}(t) = M\boldsymbol{P}(t) \tag{2.7}$$

where $\boldsymbol{P}(t) = (P_1(t), ..., P_N(t))$ is a column vector and M is a $N \times N$-matrix with the transition rates, M_{kl}, as elements. The probabilities are required to be normalized, i.e. $\sum_k P_k(t) = 1$, and $0 \leq P_k(t) \leq 1$ for all k. As a consequence, the elements of each column in M sum up to zero, which of course can be seen directly from Eq. (2.6). A general expression for the diagonal elements is given by

$$M_{kk} = -\sum_{l=1, l\neq k}^{N} M_{lk}. \tag{2.8}$$

2.3.1 Rate equation for the double QD system

The probabilities of occupying the three different states, $|00\rangle$, $|10\rangle$ and $|01\rangle$, of the double QD system are given by P_{00}, P_{10} and P_{01}, respectively. The following rate equation describes the dynamics of these probabilities,

$$\frac{d}{dt}\begin{bmatrix} P_{00} \\ P_{10} \\ P_{01} \end{bmatrix} = \begin{bmatrix} -\gamma_L & 0 & \gamma_R \\ \gamma_L & -\gamma & 0 \\ 0 & \gamma & -\gamma_R \end{bmatrix} \begin{bmatrix} P_{00} \\ P_{10} \\ P_{01} \end{bmatrix}, \tag{2.9}$$

where γ_L is the left transition rate for $|00\rangle \rightarrow |10\rangle$, γ is the transition rate for $|10\rangle \rightarrow |01\rangle$, and γ_R is the right transition rate for $|01\rangle \rightarrow |00\rangle$. The left and right transition rates can be written as

$$\gamma_L = \Gamma_L f_L(\epsilon_0) = \Gamma_L \big(e^{(\epsilon_0 - \mu_L)/k_B T} + 1\big)^{-1} \tag{2.10a}$$

$$\gamma_R = \Gamma_R \big(1 - f_R(\epsilon_0)\big) = \Gamma_R \big(e^{-(\epsilon_0 - \mu_R)/k_B T} + 1\big)^{-1} \tag{2.10b}$$

where Γ_L is the tunneling rate for electrons going from the left reservoir to the left QD, and Γ_R is, similarly, the tunneling rate for electrons going from the right QD to the right reservoir. The transition rate γ can be understood as the tunneling rate going from the left to the right QD. The Fermi functions, $f_L(\epsilon_0)$ and $f_R(\epsilon_0)$, are given by Eq. (2.1).

Equation 2.9 does not account for electron transitions in the direction towards the left reservoir. In other words, it is assumed that the Maxwell demon makes perfect, real time measurements, and operates the energy levels of the QDs infinitely fast. It should therefore be noted that Eq. (2.9) describes the complete system under ideal conditions.

2.4 Full counting statistics

Full counting statistics (FCS) is a method, for calculating electronic currents and current fluctuations, that was introduced by Levitov *et al.* [20]. The method is centered around the probability distribution $p(n, t)$ that describes the number of electrons, n, that have been transferred through a conductor within the time t. The first four cumulants of this distribution correspond to the mean, variance, skewness and kurtosis of the distribution near its maximum. The cumulants of any probability distribution are defined as the coefficients of the series expansion of the cumulant generating function, and the cumulant generating function is defined as the logarithm of the moment generating function. The mean and the variance of $p(n, t)$ are related to the current and current fluctuations,

respectively. Below is a theoretical discussion on how FCS can be implemented into rate and master equations. A similar discussion can be found in [21] or [22].

The rate equation says nothing about the number of particles that have passed through the system, therefore we denote by $P_k^{(n)}(t)$ the probability of occupying the state k when n particles have been transferred through the system since the initial time $t_0 = 0$. By defining $\boldsymbol{\rho}^{(n)}(t) \equiv \left(P_1^{(n)}(t), ..., P_N^{(n)}(t)\right)$, the rate equation (Eq. (2.7)) can be modified as follows

$$\frac{d}{dt}\boldsymbol{\rho}^{(n)}(t) = M_0\boldsymbol{\rho}^{(n)}(t) + \mathcal{J}_+\boldsymbol{\rho}^{(n-1)}(t) + \mathcal{J}_-\boldsymbol{\rho}^{(n+1)}(t), \tag{2.11}$$

where $\mathcal{J}_{+(-)}$, called jump operator, increases (decreases) the number of transferred particles, and $M = M_0 + \mathcal{J}_+ + \mathcal{J}_-$. To recover the original rate equation, the probability vector $\boldsymbol{P}(t)$ in Eq. (2.7) is defined as

$$\boldsymbol{P}(t) \equiv \sum_{n=0}^{\infty} \boldsymbol{\rho}^{(n)}(t). \tag{2.12}$$

The rate equation is hence recovered by summing over n in Eq. (2.11). Furthermore, the probability distribution of the FCS is defined as

$$p(n,t) \equiv \mathrm{tr}\left[\boldsymbol{\rho}^{(n)}(t)\right] = P_1^{(n)}(t) + P_2^{(n)}(t) + \ldots + P_N^{(n)}(t), \tag{2.13}$$

where the trace is defined as the sum of all elements in $\boldsymbol{\rho}^{(n)}(t)$.

By introducing the function

$$\boldsymbol{g}(\chi,t) \equiv \sum_n \boldsymbol{\rho}^{(n)}(t)e^{in\chi} \tag{2.14}$$

with the parameter χ, known as counting field, Eq. (2.11) can be rewritten as

$$\dot{\boldsymbol{g}}(\chi,t) = \mathcal{L}(\chi)\boldsymbol{g}(\chi,t), \tag{2.15}$$

with formal solution

$$\boldsymbol{g}(\chi,t) = e^{\mathcal{L}(\chi)t}\boldsymbol{g}(\chi,0) \tag{2.16}$$

where the matrix $\mathcal{L}(\chi) = M_0 + e^{i\chi}\mathcal{J}_+ + e^{-i\chi}\mathcal{J}_-$ is called the Liouvillian. The initial condition $\boldsymbol{\rho}^{(n)}(t=0) = \delta_{n,0}\boldsymbol{P}(t=0)$ is commonly chosen such that zero particles have passed through the system at $t = 0$. The resulting initial condition for $\boldsymbol{g}(\chi,t)$ then becomes $\boldsymbol{g}(\chi,0) = \boldsymbol{P}(0)$ where $\boldsymbol{P}(0)$ specifies the initial state of the system.

From the definition of $\boldsymbol{g}(\chi,t)$, in Eq. (2.14), it is evident that the probability distribution of the FCS is given by

$$p(n,t) = \frac{1}{2\pi}\int_{-\pi}^{\pi} \mathrm{tr}\left[\boldsymbol{g}(\chi,t)\right]e^{-in\chi}d\chi \tag{2.17}$$

where $\mathrm{tr}\left[\boldsymbol{g}(\chi,t)\right]$, by definition, is the characteristic function of $p(n,t)$. By computing the trace of Eq. (2.14), it can be seen directly that the characteristic function is given by

$$\mathcal{M}(\chi,t) \equiv \mathrm{tr}\left[\boldsymbol{g}(\chi,t)\right] = \sum_n p(n,t)e^{in\chi}. \tag{2.18}$$

The k:th moment of $p(n,t)$ is given by

$$\langle n^k(t)\rangle = (-i)^k \frac{\partial^k}{\partial \chi^k} \mathcal{M}(\chi, t)\Big|_{\chi=0}. \tag{2.19}$$

Furthermore, the cumulant generating function is given by $\mathcal{C}(\chi, t) \equiv \ln\left[\mathcal{M}(\chi, t)\right]$ and the cumulants are calculated via

$$\langle\langle n^k(t)\rangle\rangle = (-i)^k \frac{\partial^k}{\partial \chi^k} \mathcal{C}(\chi, t)\Big|_{\chi=0}. \tag{2.20}$$

The current cumulants are, in turn, obtained by differentiating Eq. (2.20) with respect to time,

$$\langle\langle I^k\rangle\rangle = \frac{d}{dt}\langle\langle n^k(t)\rangle\rangle, \tag{2.21}$$

where the mean current and current fluctuations are given for $k = 1$ and $k = 2$, respectively.

Here, we are interested in the cumulants in the long time limit for the case when there only exists one unique steady state of the rate equation (Eq. (2.7)). Equation (2.15) reduces to the rate equation when we chose $\chi = 0$, and from the rate equation we see that $\mathcal{L}(\chi)$ must have one eigenvalue $\lambda(\chi)$, for which $\lambda(0) = 0$, with a corresponding, non-zero eigenvector. Furthermore, with $Q(\chi)$ being the matrix diagonalizing $\mathcal{L}(\chi)$, the moment generating function can, by using Eq. (2.16), be written as

$$\mathcal{M}(\chi, t) = \mathrm{tr}\left[e^{Q(\chi)\mathcal{L}_D(\chi)Q^{-1}(\chi)t} g(\chi, 0)\right], \tag{2.22}$$

where $\mathcal{L}_D(\chi)$ is the diagonal form of $\mathcal{L}(\chi)$. Since we are looking at the case with only one unique steady state, all other eigenvalues than $\lambda(\chi)$ must have a non-vanishing negative real part near $\chi = 0$ [22]. It is assumed that all eigenvalues have a negative real part for finite χ where the real part of $\lambda(\chi)$ is the largest [22]. Then we observe that the moment generating function $\mathcal{M}(\chi, t) \to e^{\lambda(\chi)t} c(\chi)$ in the long time limit, where $c(\chi)$ is a polynomial depending on $Q(\chi)$. Hence, we can approximate the cumulant generating function by

$$\mathcal{C}(\chi, t) \approx \lambda(\chi) t \tag{2.23}$$

in the long time limit where we neglect the term $\ln\big(c(\chi)\big)$. By neglecting this term, the cumulant generating function is determined up to a small correction. This correction is, however, negligible when calculating the current cumulants since $\ln\big(c(\chi)\big)$ is time independent. Hence, in the long time limit, Eq. (2.17) can be approximated with

$$p(n, t) \xrightarrow{\text{large t}} \frac{1}{2\pi} \int_{-\pi}^{\pi} e^{\lambda(\chi)t} e^{-in\chi} d\chi, \tag{2.24}$$

and the cumulants are given by

$$\langle\langle n^k(t)\rangle\rangle \xrightarrow{\text{large t}} (-i)^k \frac{\partial^k}{\partial \chi^k} \lambda(\chi)\Big|_{\chi=0} t. \tag{2.25}$$

From Eq. (2.25), it is evident that the cumulants are linear in time in the long time limit. It should, however, be noted that the above discussion only holds when a system has a unique steady state; for systems with multiple steady states, other methods are needed [22, 23, 24].

2.4.1 Full counting statistics in the double QD system

When applying FCS to the double QD system, the following Liouvillian is obtained,

$$\mathcal{L}(\chi) = M_0 + e^{i\chi}\mathcal{J}_+ = \begin{bmatrix} -\gamma_L & 0 & e^{i\chi}\gamma_R \\ \gamma_L & -\gamma & 0 \\ 0 & \gamma & -\gamma_R \end{bmatrix}, \tag{2.26}$$

where only the jump operator $\mathcal{J}_+$ is present since electrons only are transferred towards the right reservoir, i.e. the number of transferred particles cannot be decreased. The transition rate $\gamma_{L(R)}$ represents the transition of electrons between the left(right) reservoir and the left(right) QD. The transition rates are given by Eqs. (2.10). The initial condition for Eq. (2.15) is chosen as $g(\chi, 0) = (1, 0, 0)$ such that the double QD system is prepared to initially be in the state $|00\rangle$ with zero electrons transferred to the right reservoir.

2.5 Monte Carlo simulation

This section presents the Monte Carlo method that was used to simulate the dynamics of the complete system.

As was pointed out in Sec. 2.1, the double quantum dot system can be in the following states: $|00\rangle$; $|10\rangle$; and $|01\rangle$, and the only transitions possible are $|00\rangle \to |10\rangle \to |01\rangle \to |00\rangle$. Let the index $i = 0, 1, 2$ represent the states $|00\rangle$, $|10\rangle$, and $|01\rangle$, respectively. Thus, if $|i\rangle$ is occupied, the only possible transition is to $|i+1\rangle$; e.g. if $i = 2$, $i + 1 = 0$. If the state $|i\rangle$ is occupied at the time t, the probability of being in $|i+1\rangle$ at the time $t + \delta t$ is given by $P_{i+1}(t + \delta t) = \delta t \Gamma_{|i+1\rangle,|i\rangle}$, where $\Gamma_{|i+1\rangle,|i\rangle}$ is the transition rate going from $|i\rangle$ to $|i+1\rangle$, and δt is chosen such that $\delta t \Gamma_{|i+1\rangle,|i\rangle} \ll 1$. By $P_i(t + \delta t)$, we denote the probability to stay in $|i\rangle$ after the time $t + \delta t$, and the total probability at this time must be $P_{i+1}(t + \delta t) + P_i(t + \delta t) = 1$. If a closed interval between 0 and 1 is considered, we can assign the subinterval $[0, \delta t \Gamma_{|i+1\rangle,|i\rangle}]$ to the probability $P_{i+1}(t + \delta t)$. When drawing a random number $\epsilon \in [0, 1]$, we say that the transition from $|i\rangle$ to $|i+1\rangle$ occurs if $\epsilon \in [0, \delta t \Gamma_{|i+1\rangle,|i\rangle}]$. If $\epsilon \notin [0, \delta t \Gamma_{|i+1\rangle,|i\rangle}]$, the system stays in $|i\rangle$. Therefore, the following steps were used to simulate the dynamics of the complete system:

1. Start in $|00\rangle$.
2. Generate a random number $\epsilon \in [0, 1]$, and increase time by δt.
3. If $\epsilon \in [0, \delta t \Gamma_{|10\rangle,|00\rangle}]$ go to $|10\rangle$, otherwise go back to step 2.
4. Generate a random number $\epsilon \in [0, 1]$, and increase time by δt.
5. If $\epsilon \in [0, \delta t \Gamma_{|01\rangle,|10\rangle}]$ go to $|01\rangle$, otherwise go back to step 4.
6. Generate a random number $\epsilon \in [0, 1]$, and increase time by δt.
7. If $\epsilon \in [0, \delta t \Gamma_{|00\rangle,|01\rangle}]$ go to $|00\rangle$ and start over from step 1, otherwise go back to step 6.

Chapter 3

Results and discussion

In this chapter, the solutions and results of the equations and methods set up in chapter 2 are presented and discussed. Section 3.1 is devoted to rate equations, and Sec. 3.2 to full counting statistics (FCS). The FCS is treated both analytically and numerically. In Sec. 3.3, the Monte Carlo simulation of the complete system is compared to the FCS.

3.1 Rate equation

From the rate equation given by Eq. (2.9) in Sec. 2.3.1, the following differential equations can be obtained

$$\frac{dP_{10}}{dt} = \big(\gamma + \Gamma_L f_L(\epsilon_0)\big)P_{10} - \Gamma_L f_L(\epsilon_0) - \Gamma_L f_L(\epsilon_0)P_{01}, \tag{3.1a}$$

$$\frac{dP_{01}}{dt} = \Gamma_R\big(1 - f_R(\epsilon_0)\big)P_{01} + \gamma P_{10}, \tag{3.1b}$$

where $P_{00} = 1 - P_{10} - P_{01}$, and the transition rates $\gamma_L = \Gamma_L f_L(\epsilon_0)$ and $\gamma_R = \Gamma_R\big(1 - f_R(\epsilon_0)\big)$, given by Eqs. (2.10), have been used. The steady state solution of these equations are

$$P_{00} = \frac{\gamma\Gamma_R\big(1 - f_R(\epsilon_0)\big)}{\gamma\big(\Gamma_R + \Gamma_L f_L(\epsilon_0) - \Gamma_R f_R(\epsilon_0)\big) + \Gamma_L\Gamma_R f_L(\epsilon_0)\big(1 - f_R(\epsilon_0)\big)}, \tag{3.2a}$$

$$P_{10} = \frac{\Gamma_L\Gamma_R f_L(\epsilon_0)\big(1 - f_R(\epsilon_0)\big)}{\gamma\big(\Gamma_R + \Gamma_L f_L(\epsilon_0) - \Gamma_R f_R(\epsilon_0)\big) + \Gamma_L\Gamma_R f_L(\epsilon_0)\big(1 - f_R(\epsilon_0)\big)}, \tag{3.2b}$$

$$P_{01} = \frac{\gamma\Gamma_L f_L(\epsilon_0)}{\gamma\big(\Gamma_R + \Gamma_L f_L(\epsilon_0) - \Gamma_R f_R(\epsilon_0)\big) + \Gamma_L\Gamma_R f_L(\epsilon_0)\big(1 - f_R(\epsilon_0)\big)}. \tag{3.2c}$$

By considering the techniques used in [25], it is possible to show that the form of Eqs. (3.2) is general for systems like the one discussed in this thesis [26] which include a finite number of states $|j\rangle$, $j = 1, 2, ..., N$, where the only transitions allowed are $|j\rangle \to |j+1\rangle$ for all j, where $|N+1\rangle = |1\rangle$.

The absolute charge on the left and right QDs are given by

$$Q_{DL} = eP_{10}(t) \text{ and } Q_{DR} = eP_{01}(t), \tag{3.3}$$

where e is the elementary charge, here taken as a positive quantity. The time derivatives of these two equations are given by

$$\frac{dQ_{DL}}{dt} = e\frac{dP_{10}}{dt} = I_L - I_S, \tag{3.4a}$$
$$\frac{dQ_{DR}}{dt} = e\frac{dP_{01}}{dt} = I_S - I_R, \tag{3.4b}$$

where I_L is the current between the left reservoir and the left QD, I_S is the current between the QDs, and I_R is the current between the right reservoir and the right QD. The sign convention used here is chosen such that currents are positive when electrons are moving from left to right, and negative in the opposite case. Putting Eqs. (3.1) into Eqs. (3.4), one gets the following expressions for the currents,

$$I_L = e\Gamma_L f_L(\epsilon_0)P_{00}, \tag{3.5a}$$
$$I_S = e\gamma P_{10}, \tag{3.5b}$$
$$I_R = e\Gamma_R\big(1 - f_R(\epsilon_0)\big)P_{01}. \tag{3.5c}$$

Using Eqs. (3.2), (3.4) and (3.5), we obtain the steady state current $I = I_L = I_S = I_R$ which is given by

$$\begin{aligned} I &= \frac{e\gamma\Gamma_L\Gamma_R f_L(\epsilon_0)\big(1 - f_R(\epsilon_0)\big)}{\gamma\big(\Gamma_R + \Gamma_L f_L(\epsilon_0) - \Gamma_R f_R(\epsilon_0)\big) + \Gamma_L\Gamma_R f_L(\epsilon_0)\big(1 - f_R(\epsilon_0)\big)} \\ &= \frac{e\gamma\gamma_L\gamma_R}{\gamma\gamma_L + \gamma\gamma_R + \gamma_L\gamma_R}. \end{aligned} \tag{3.6}$$

After the second equality, we have expressed the current in terms of the transition rates $(\gamma, \gamma_L, \gamma_R)$ given in Sec. 2.3.1. Through an Ohm's law-like relation, Eq. (3.6) can be interpreted as the current in an electric circuit with three resistors coupled in series. The resistors correspond to the three tunnel barriers in the complete system. If the resistance of the tunnel barriers are given by $R_L \propto 1/\gamma_L$, $R_\gamma \propto 1/\gamma$ and $R_R \propto 1/\gamma_R$, with V/e as proportionality constant in the linear response regime, where V is the voltage bias, the total resistance would be $R_{tot} = R_L + R_\gamma + R_R$. In an Ohmic circuit, the current is proportional to $1/R_{tot}$, and for our case, we get back the current given above when calculating $1/R_{tot}$. It should be stressed that Ohm's law does not hold in general for the double QD system, see Fig. 3.1. However, for small voltage biases, or high temperatures, Ohm's law is valid in the complete system.

The current is plotted in Fig. 3.1 in dimensionless units as a function of eV/k_BT where $eV = \mu_L - \mu_R$ is the voltage bias between the left and right reservoirs. In the plot, the left and right tunneling rates are chosen to be equal, $\Gamma = \Gamma_L = \Gamma_R$, and $\Gamma/\gamma = 0.5$. The chemical potentials are further chosen symmetrically around ϵ_0 as $\mu_L = \epsilon_0 + eV/2$ and $\mu_R = \epsilon_0 - eV/2$; $\epsilon_0 = 0$ is used here without loss of generality. Most interesting in the plot is the positive current for negative voltage bias where electrons are transported towards the right reservoir that has the higher chemical potential. This proves that the Maxwell demon works properly. As the negative voltage bias becomes large, the current tends to zero. For large negative voltage bias, and symmetrically chosen chemical potentials,

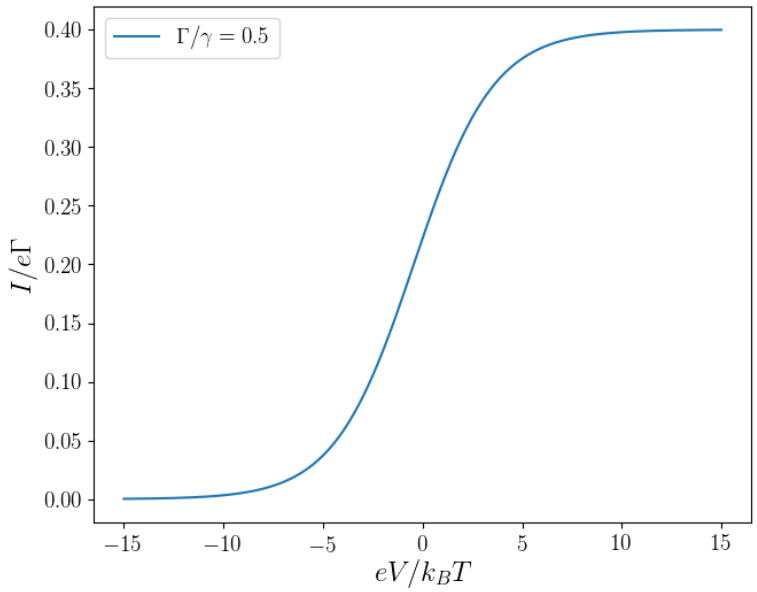

Figure 3.1: *Current given by Eq. (3.6) in dimensionless units as a function of* eV/k_BT. *Here,* V *is the voltage bias between the left and right reservoirs given by* $eV = \mu_L - \mu_R$. *The chemical potentials are chosen symmetrically around* ϵ_0 *such that* $\mu_L = \epsilon_0 + eV/2$ *and* $\mu_R = \epsilon_0 - eV/2$. *For this plot,* $\epsilon_0 = 0$. *The left and right tunneling rates are here chosen to be equal,* $\Gamma = \Gamma_L = \Gamma_R$, *and* $\Gamma/\gamma = 0.5$.

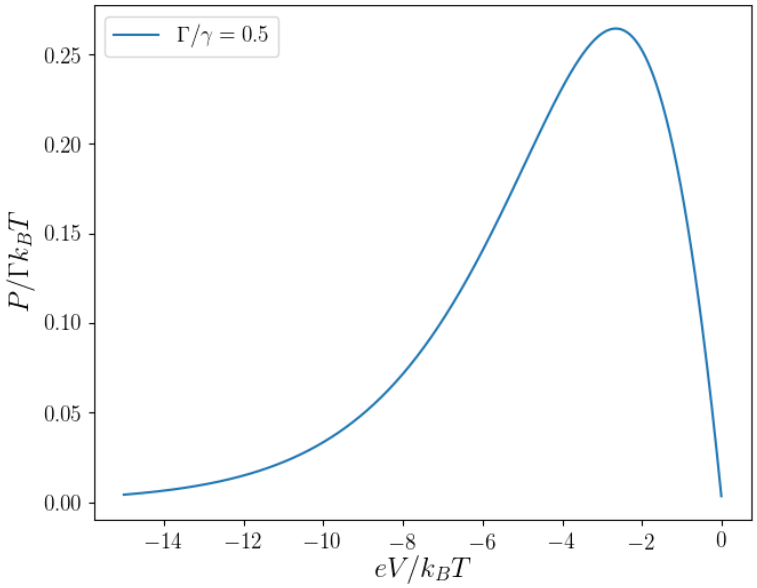

Figure 3.2: *The electrical power of the current in Fig. 3.1. Here, the power is given in dimensionless units as a function of* eV/k_BT. *The power for positive voltage bias is omitted since it is unrelated to the operations of the Maxwell demon.*

the Fermi functions of the reservoirs take the values $f_L(\epsilon_0) = 0$ and $f_R(\epsilon_0) = 1$, respectively. As a result, no electrons can be transported through the system. Similarly, for large positive voltage bias, the current becomes constant. This is due to the fact that the Fermi functions of the reservoirs take the values $f_L(\epsilon_0) = 1$ and $f_R(\epsilon_0) = 0$.

By defining the electrical power as $P = -V \cdot I$, the power becomes positive when the current runs against the voltage bias, i.e. when $V < 0$. The power is therefore negative when the current is running in the direction of the voltage bias. The power can in general be positive for $V > 0$, but in the double QD system, the currents are only traveling from left to right, and hence, the reasoning above holds true. Figure 3.2 displays the power of the current given in Fig. 3.1 in dimensionless units. The power for positive voltage bias is omitted in the figure since it is unrelated to the operations of the Maxwell demon.

The electrical power is given, in terms of $\gamma k_B T$, by

$$\frac{P}{\gamma k_B T} = -\frac{eV}{k_B T} \frac{(\Gamma_L/\gamma)(\Gamma_R/\gamma) f_L(\epsilon_0)\big(1 - f_R(\epsilon_0)\big)}{(\Gamma_L/\gamma) f_L(\epsilon_0) + (\Gamma_R/\gamma)\big(1 - f_R(\epsilon_0)\big) + (\Gamma_L/\gamma)(\Gamma_R/\gamma) f_L(\epsilon_0)\big(1 - f_R(\epsilon_0)\big)}, \tag{3.7}$$

where Γ_L/γ and Γ_R/γ are dimensionless tunneling rates. In Fig. 3.3, three examples of this dimensionless power are visualized as a function of the dimensionless quantities $\epsilon_0/k_B T$ and $eV/k_B T$. The chemical potentials are chosen as $\mu_L = eV/2$ and $\mu_R = -eV/2$.

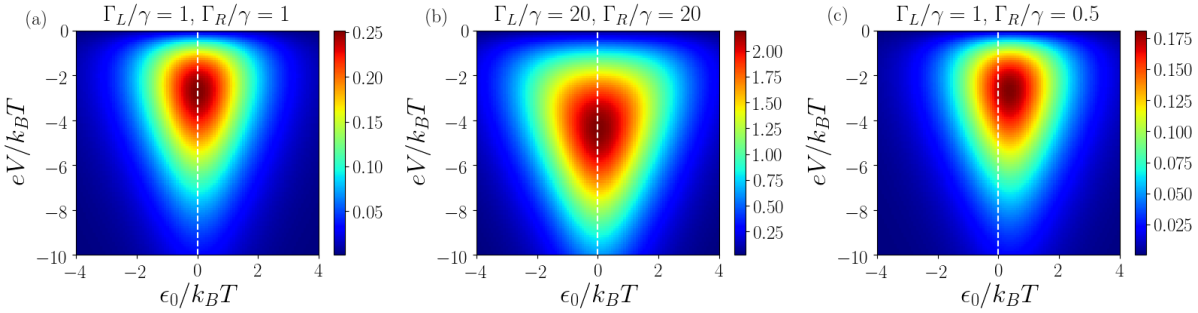

Figure 3.3: *The power given by Eq. (3.7) as a function of $\epsilon_0/k_B T$ and $eV/k_B T$. The chemical potentials are chosen as $\mu_L = eV/2$ and $\mu_R = -eV/2$. Three examples are given in the figure for different dimensionless tunneling rates Γ_L/γ and Γ_R/γ: (a) $\Gamma_L/\gamma = \Gamma_R/\gamma = 1$; (b) $\Gamma_L/\gamma = \Gamma_R/\gamma = 20$; and (c) $\Gamma_L/\gamma = 1$, $\Gamma_R/\gamma = 0.5$. The line $\epsilon_0/k_B T = 0$ is marked as a white, dashed line.*

As can be seen in Figs. 3.3a and 3.3b for $\Gamma_L/\gamma = \Gamma_R/\gamma$, the power is symmetric around the line $\epsilon_0/k_B T = 0$. This symmetry represents the transform $\epsilon_0/k_B T \to -\epsilon_0/k_B T$ in Eq. (3.7) which in this case corresponds to exchanging $\gamma_L \leftrightarrow \gamma_R$. It is clear from Figs. 3.3a and 3.3b that if the dimensionless tunneling rates are increased, then so is the power. Noticeable is that the general shape of the power is stretched, and that the position where the maximum is attained moves along the line $\epsilon_0/k_B T = 0$ as the transition rates are increased. However, if the tunneling rates are non-equal, the maximum is no longer positioned on the line $\epsilon_0/k_B T = 0$. This effect can clearly be seen in Fig. 3.3c. The

positions where the maxima occur are given by

$$\frac{\epsilon_0}{k_BT} = \frac{1}{2}\ln\left[\frac{\Gamma_L}{\Gamma_R}\right] \tag{3.8a}$$

$$\frac{eV}{k_BT} = -2\Big[W\Big(\frac{(\Gamma_L/\gamma)+(\Gamma_R/\gamma)+(\Gamma_L/\gamma)(\Gamma_R/\gamma)}{2e\sqrt{(\Gamma_L/\gamma)(\Gamma_R/\gamma)}}\Big)+1\Big] \tag{3.8b}$$

where $W(z)$ is the Lambert W function, also called the product logarithm function, which fulfills $z = W(ze^z)$. Note that the e in Eq. (3.8b) is Euler's number and not the elementary charge. When looking at these equations, it is evident that for equal tunneling rates, $\Gamma_L = \Gamma_R$, the maximum occurs along the line $\epsilon_0/k_BT = 0$, and this clearly agrees with Figs. 3.3a and 3.3b. Equations 3.8 also predict the maximum of the power in Fig. 3.2 which occurs at $eV/k_BT \sim -2.6$.

3.2 Full counting statistics

This section is divided into three parts. In Sec. 3.2.1, the analytical results of the simplest case, where $\gamma = \gamma_L = \gamma_R$, are presented. A more general case, where $\gamma \neq \gamma_L \neq \gamma_R$, is evaluated analytically in Sec. 3.2.2. Furthermore, a numerical study of the FCS was performed, with the results displayed in Sec. 3.2.3.

3.2.1 Analytic Case I: All transition rates equal

With all transition rates equal, $\gamma = \gamma_L = \gamma_R$, the following Liouvillian is obtained

$$\mathcal{L}(\chi) = \begin{bmatrix} -\gamma & 0 & e^{i\chi}\gamma \\ \gamma & -\gamma & 0 \\ 0 & \gamma & -\gamma \end{bmatrix}, \tag{3.9}$$

with eigenvalues

$$\lambda_l(\chi) = \gamma(e^{i\chi/3}e^{2\pi li/3} - 1),\ l = 0, 1, 2. \tag{3.10}$$

The eigenvalue for $l = 0$ is zero for $\chi = 0$, and is hence, as seen in Eq. (2.23), the eigenvalue that approximates the cumulant generating function in the long time limit,

$$\mathcal{C}(\chi, t) \approx \gamma(e^{i\chi/3} - 1)\cdot t. \tag{3.11}$$

A general expression for the k:th order cumulant is given by

$$\langle\langle n^k\rangle\rangle = \frac{\gamma t}{3^k},\ k = 1, 2, 3, ... \tag{3.12}$$

The cumulants normalized by $\langle\langle n\rangle\rangle$ are calculated via $\langle\langle n^k\rangle\rangle/\langle\langle n\rangle\rangle = 1/3^{k-1}$. For $k = 2$, we get the Fano factor $\langle\langle n^2\rangle\rangle/\langle\langle n\rangle\rangle = 1/3$, and the normalized third cumulant ($k = 3$) becomes $\langle\langle n^3\rangle\rangle/\langle\langle n\rangle\rangle = 1/9$. It can be noted that the normalized cumulants are constants, and independent of any of the parameters in the double QD system. It should be noted that the Fano factor is defined as $F = \sigma^2/\mu$ with σ^2 being the variance of a distribution and μ its mean. From this factor, we can read off information about a distribution. For a Poisson distribution, $F = 1$ since $\sigma^2 = \mu$. A distribution with $F > 1$ or $F < 1$ is said to be

super- or sub-Poissonian, respectively. When studying electron transport, the two cases correspond to electrons coming in bunches or separately. For the case with $\gamma = \gamma_L = \gamma_R$, the electron transport is sub-Poissonian.

The current cumulants are simply obtained by differentiating Eq. (3.12) with respect to time, $\langle\langle I^k \rangle\rangle = \gamma/3^k$, see Eq. (2.21).

In the long time limit, the probability distribution, $p(n,t)$, can be evaluated with Eq. (2.24) using the saddle point approximation method. The resulting distribution is given by (derivation in Appendix A)

$$p(n,t)_{\gamma=\gamma_L=\gamma_R} \approx \sqrt{\frac{3}{2\pi n}}\left(\frac{\gamma t e}{3n}\right)^{3n} e^{-\gamma t}. \tag{3.13}$$

The shape of Eq. (3.13) can emerge from a Poisson distribution

$$(\gamma t)^N e^{-\gamma t}/N!, \tag{3.14}$$

by using Stirling's approximation, $N! \sim \sqrt{2\pi N}(N/e)^N$. Eq. (3.14) can then be written as

$$\frac{1}{\sqrt{2\pi N}}\left(\frac{\gamma t e}{N}\right)^N e^{-\gamma t}. \tag{3.15}$$

It should be noted that the discrete variable N is considered to be continuous after applying Stirling's approximation. Therefore, the variable exchange $N = 3n$ gives back Eq. (3.13). The application of Stirling's approximation can be justified if we assume that a large number of electrons, $N = 3n$, have been transferred through the system in the long time limit. Furthermore, the $3n$ in Eq. (3.13) corresponds to the electrons having to tunnel three times before reaching the right reservoir.

3.2.2 Analytic Case II: General case

In this section, the results for the case when the transition rates are non-equal are presented. The Liouvillian for this case is given by Eq. (2.26) and has the characteristic polynomial

$$\lambda^3 + \lambda^2(\gamma + \gamma_L + \gamma_R) + \lambda(\gamma\gamma_L + \gamma\gamma_R + \gamma_L\gamma_R) + \gamma\gamma_L\gamma_R(1 - e^{i\chi}) = 0. \tag{3.16}$$

It should be noted that this polynomial has a symmetry; it is invariant under the exchange of any two transition rates.

As was pointed out in Sec. 2.4, the cumulant generating function can be approximated with the eigenvalue of the Liouvillian which vanishes for $\chi = 0$. The eigenvalues of the Liouvillian are accessible as the solutions of Eq. (3.16), but results in cumbersome expressions. In this thesis, however, we circumvent these cumbersome expressions by utilizing the following method.

Denote by $\lambda_1(\chi)$ the eigenvalue of the Liouvillian that satisfies $\lambda_1(\chi = 0) = 0$. If $\lambda_1(\chi)$ is put into the characteristic polynomial, we get the following when differentiating with respect to χ,

$$3\lambda_1^2\frac{d\lambda_1}{d\chi} + 2\lambda_1\frac{d\lambda_1}{d\chi}(\gamma + \gamma_L + \gamma_R) + \frac{d\lambda_1}{d\chi}(\gamma\gamma_L + \gamma\gamma_R + \gamma_L\gamma_R) - i\gamma\gamma_L\gamma_R e^{i\chi} = 0. \tag{3.17}$$

By putting $\chi = 0$, the following expression for the first derivative at $\chi = 0$ is obtained,

$$\left.\frac{d\lambda_1}{d\chi}\right|_{\chi=0} = i\frac{\gamma\gamma_L\gamma_R}{\gamma\gamma_L + \gamma\gamma_R + \gamma_L\gamma_R}, \tag{3.18}$$

and from Eq. (2.25), we obtain the first cumulant in the long time limit,

$$\langle\langle n\rangle\rangle = \frac{\gamma\gamma_L\gamma_R}{\gamma\gamma_L + \gamma\gamma_R + \gamma_L\gamma_R}t. \tag{3.19}$$

To get the second cumulant, one needs to differentiate Eq. (3.17) with respect to χ, and then put $\chi = 0$. From this stage, one can derive an expression for the second derivative at $\chi = 0$, and with the help of Eq. (2.25) we arrive at the second cumulant. The method is able to generate cumulants of any order, and below are the second and third cumulants,

$$\langle\langle n^2\rangle\rangle = \gamma\gamma_L\gamma_R\frac{(\gamma\gamma_L + \gamma\gamma_R + \gamma_L\gamma_R)^2 - 2\gamma\gamma_L\gamma_R(\gamma + \gamma_L + \gamma_R)}{(\gamma\gamma_L + \gamma\gamma_R + \gamma_L\gamma_R)^3}t, \tag{3.20}$$

and

$$\begin{aligned}\langle\langle n^3\rangle\rangle = \gamma\gamma_L\gamma_R\Big((\gamma\gamma_L + \gamma\gamma_R + \gamma_L\gamma_R)^4 - 6\gamma^2\gamma_L^2\gamma_R^2(\gamma\gamma_L + \gamma\gamma_R + \gamma_L\gamma_R) \\ - 6\gamma\gamma_L\gamma_R(\gamma + \gamma_L + \gamma_R)\Big[(\gamma\gamma_L + \gamma\gamma_R + \gamma_L\gamma_R)^2 - 2\gamma\gamma_L\gamma_R(\gamma + \gamma_L + \gamma_R)\Big]\Big)t \Big/ \\ (\gamma\gamma_L + \gamma\gamma_R + \gamma_L\gamma_R)^5.\end{aligned} \tag{3.21}$$

An expression for the fourth cumulant is given in Appendix B.

The Fano factor for the general case has a lower and upper bound that are given by

$$\frac{1}{3} \leq \frac{\langle\langle n^2\rangle\rangle}{\langle\langle n\rangle\rangle} \leq 1. \tag{3.22}$$

The lower bound corresponds to the case where all transition rates are equal, $\gamma = \gamma_L = \gamma_R$, and this agrees with the results of Sec. 3.2.1. In addition, the second inequality in Eq. (3.22) provides the upper bound 1 for the Fano factor indicating that the system is sub-Poissonian when the inequality is strict. Sub-Poissonian means that electrons travel one-by-one instead of coming in bunches, and this is what we expect for fermions. When the Fano factor is 1, the system follows Poissonian statistics; this is the case when any two transition rates are much larger than the third rate.

When Eq. (3.19) is differentiated with respect to time, the mean current is obtained,

$$\langle\langle I\rangle\rangle = \frac{\gamma\gamma_L\gamma_R}{\gamma\gamma_L + \gamma\gamma_R + \gamma_L\gamma_R}, \tag{3.23}$$

and this is the same current that was obtained in Sec. 3.1. By choosing the transitions rates as $\gamma_L = \Gamma_L f_L(\epsilon_0)$ and $\gamma_R = \Gamma_R\big(1 - f_R(\epsilon_0)\big)$ (see Eqs. (2.10)), Eq. (3.6) is recovered.

When putting $\gamma = \gamma_L = \gamma_R$ in Eqs. (3.19)-(3.21) and (B.1), the results given by Eq. (3.12) are recovered. This acts as a sanity check verifying that the different approaches yield the same results.

When a bottleneck is introduced in the system, for example by having $\gamma \ll \gamma_L, \gamma_R$, the system follows Poissonian statistics. If it is assumed that γ is a small quantity such that $\gamma^r \approx 0$ for $r > 1$, the eigenvalues $\lambda(\chi)$ in Eq. (3.16) can be approximated with

$$\lambda(\chi) \approx a_0(\chi) + a_1(\chi)\gamma \tag{3.24}$$

where $a_0(\chi)$ and $a_1(\chi)$ are functions of χ, γ_L and γ_R fulfilling $a_0(0) = a_1(0) = 0$ such that $\lambda(0) = 0$. By plugging Eq. (3.24) into Eq. (3.16) and neglecting all higher order terms in γ, we get $a_0(\chi) = 0$ and $a_1(\chi) = e^{i\chi} - 1$ such that $\lambda(\chi) = \gamma(e^{i\chi} - 1)$. Equation (2.24) then gives the following distribution in the long time limit,

$$p(n,t) = \frac{(\gamma t)^n}{n!} e^{-\gamma t}. \tag{3.25}$$

This shows that the complete system is Poissonian when $\gamma \ll \gamma_L, \gamma_R$. It should be noted that the system follows Poissonian statistics when any transition rate is much smaller than the others; the arguing above holds for any of the three transition rates.

Figure 3.4 visualizes: (a) the dimensionless first cumulant $\langle\langle n\rangle\rangle/\gamma t$; (b) the Fano factor $\langle\langle n^2\rangle\rangle/\langle\langle n\rangle\rangle$; and (c) the normalized third cumulant $\langle\langle n^3\rangle\rangle/\langle\langle n\rangle\rangle$. All quantities are plotted as functions of the dimensionless transition rates $\gamma_{L/R}/\gamma$, and the white, dashed line in each graph emphasizes where $\gamma_L = \gamma_R$. It is clear that all cumulants are mirror symmetric with respect to the line $\gamma_L = \gamma_R$, and this visualizes the symmetry of swapping $\gamma_L \leftrightarrow \gamma_R$ in Eq. (3.16). In both Figs. 3.4b and 3.4c, the regions where $\gamma = \gamma_L = \gamma_R$ clearly take the values $\langle\langle n^2\rangle\rangle/\langle\langle n\rangle\rangle = 1/3$ and $\langle\langle n^3\rangle\rangle/\langle\langle n\rangle\rangle = 1/9$ as pointed out in Sec. 3.2.1. Furthermore, Fig. 3.4b clearly fulfills the lower and upper bound given by Eq. (3.22). For the regimes where $\gamma \ll \gamma_L, \gamma_R$ it is evident that both the Fano factor and the normalized third cumulant are ~ 1, and hence, the system follows Poissonian statistics in those regimes as seen in Eq. (3.25). Furthermore, as γ is much smaller than both the left and right transition rates, the system can be viewed as a single tunnel barrier.

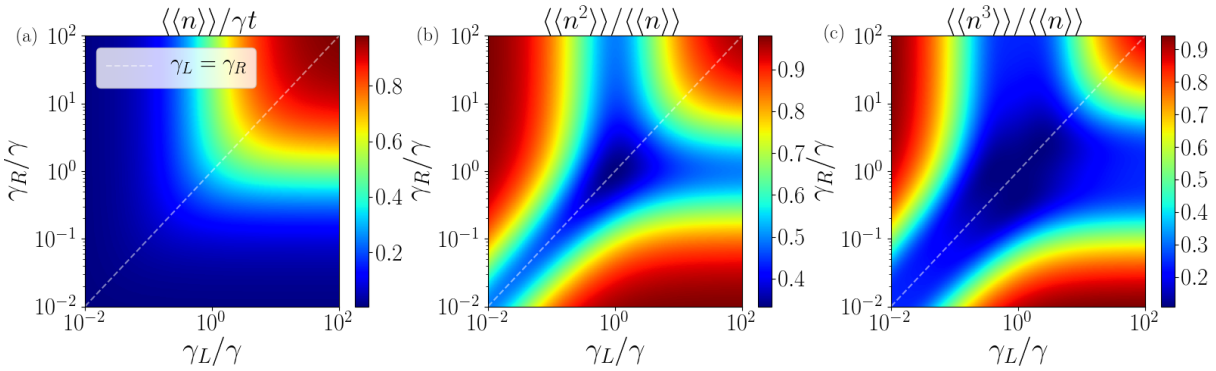

Figure 3.4: *(a) The first cumulant in dimensionless units. (b) The second cumulant normalized by $\langle\langle n\rangle\rangle$, this quantity is known as the Fano factor. (c) The third cumulant normalized by $\langle\langle n\rangle\rangle$. All cumulants are plotted as functions of γ_L/γ and γ_R/γ.*

The cumulants of the electrical power can be calculated in dimensionless units via

$$\frac{\langle\langle P^k\rangle\rangle}{\gamma(k_B T)^k} = \Big(-\frac{eV}{k_B T}\Big)^k \frac{\langle\langle n^k\rangle\rangle}{\gamma t}, \quad k = 1,2,3, \tag{3.26}$$

where the first three cumulants $\langle\langle n^k\rangle\rangle$, $k = 1,2,3$, are given by Eqs. (3.19)-(3.21). For $k = 1$, Eq. (3.7) is re-obtained if $\gamma_L = \Gamma_L f_L(\epsilon_0)$ and $\gamma_R = \Gamma_R\big(1 - f_R(\epsilon_0)\big)$ are chosen. A visualization of $\langle\langle P\rangle\rangle$ is displayed in Fig. 3.3. The second and third cumulants of the electrical power are plotted in Fig. 3.5 for the dimensionless tunneling rates $\Gamma_{L/R}/\gamma = 1$,

and the chemical potentials $\mu_L = eV/2$ and $\mu_R = -eV/2$. For the second cumulant, in Fig. 3.5a, two maxima are observed, one on each side of the line $\epsilon_0/k_BT = 0$. The maxima correspond to regions of increased variance in the probability distribution of the power. Similarly, the third cumulant in Fig. 3.5b has also two maxima, and these tell us where the probability distribution of the power has its largest skewness.

In Appendix D, the second and third cumulants are plotted for some different Γ_L/γ and Γ_R/γ. For equal and small dimensionless tunneling rates, both cumulants decrease, and $\langle\langle P^3\rangle\rangle$ is reshaped, and becomes negative in some regions. For equal, and large dimensionless tunneling rates, we observe that both $\langle\langle P^2\rangle\rangle$ and $\langle\langle P^3\rangle\rangle$ increase, and are reshaped. Finally, as the dimensionless tunneling rates are non-equal, the cumulants are reshaped and shifted with respect to the line $\epsilon_0/k_BT = 0$.

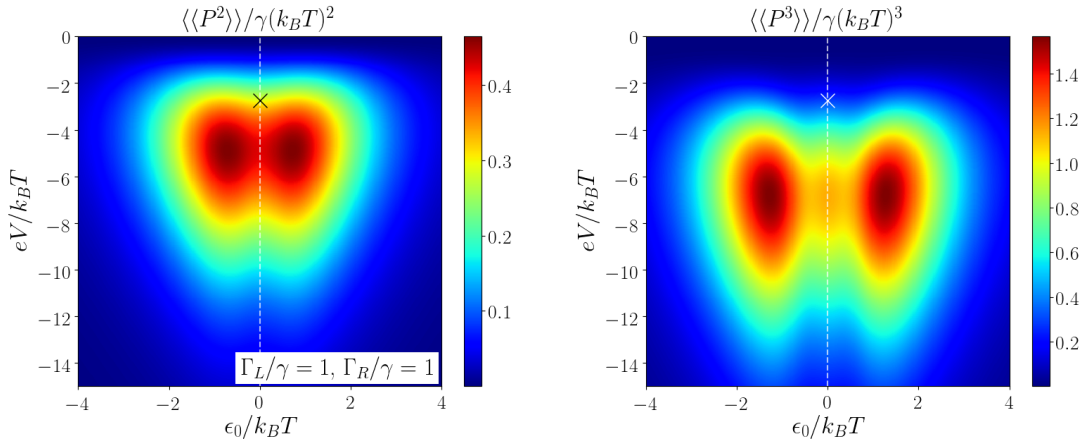

Figure 3.5: *(a) Second and (b) third cumulants of the power given in Eqs. (3.26). The cumulants are plotted as functions of ϵ_0/k_BT and eV/k_BT. The white, dashed line emphasizes the line $\epsilon_0/k_BT = 0$, and the black, or white, cross is located where the power has its maximum. The chemical potentials are here chosen as $\mu_L = eV/2$ and $\mu_R = -eV/2$.*

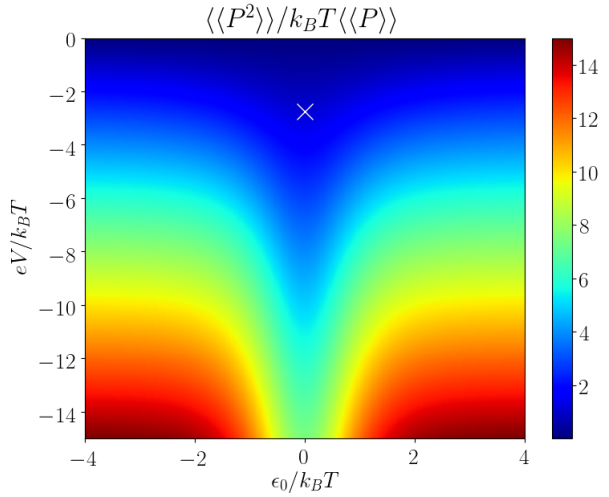

Figure 3.6: *The graph displays the quantity $\langle\langle P^2\rangle\rangle/\langle\langle P\rangle\rangle$ in terms of k_BT as a function of ϵ_0/k_BT and eV/k_BT, here for $\Gamma_L/\gamma = \Gamma_R/\gamma = 1$. The chemical potentials are here given by $\mu_L = eV/2$ and $\mu_R = -eV/2$. The white cross is located where the power has its maximum.*

Figure 3.6 displays the quantity $\langle\langle P^2\rangle\rangle/\langle\langle P\rangle\rangle$ in terms of k_BT for $\Gamma_{L/R}/\gamma = 1$. The quantity is clearly mirror symmetric with respect to the line $\epsilon_0/k_BT = 0$, this is due to that both $\langle\langle P^2\rangle\rangle$ and $\langle\langle P\rangle\rangle$ are mirror symmetric with respect to the same line, see Figs. 3.3a and 3.5a. For large negative voltage bias, i.e. $eV/k_BT \sim -14$, and $\epsilon_0/k_BT \sim |3|$, we observe two regions where $\langle\langle P^2\rangle\rangle/\langle\langle P\rangle\rangle \sim 14k_BT$. As eV/k_BT is increased, the ratio $\langle\langle P^2\rangle\rangle/\langle\langle P\rangle\rangle$ decreases, around $eV/k_BT \sim 0$, $\langle\langle P^2\rangle\rangle/\langle\langle P\rangle\rangle \sim k_BT$. For temperatures that typically are used in experiments, i.e. $T \sim 0.1$ K, $\langle\langle P^2\rangle\rangle/\langle\langle P\rangle\rangle \sim 10^{-6}$ eV.

The black and white crosses in Figs. 3.5 and 3.6 shows the location of the maximum power that is given by Eqs. (3.8). From Fig. 3.5, we see that the maximum positions for both variance and skewness do not overlap with the position of the maximum power. This means that we do not have maximum fluctuations and skewness when we have maximum power.

3.2.3 Numerics

By letting the left and right transition rates be equal, $\Omega = \gamma_L = \gamma_R$, the Liouvillian, given in Eq. (2.26), can be rewritten as

$$\frac{\mathcal{L}(\chi)}{\gamma} = \begin{bmatrix} -\Omega/\gamma & 0 & e^{i\chi}\Omega/\gamma \\ \Omega/\gamma & -1 & 0 \\ 0 & 1 & -\Omega/\gamma \end{bmatrix}, \tag{3.27}$$

where it only depends on the parameter Ω/γ. The probability distribution given by Eq. (2.17) was calculated numerically for this Liouvillian, and the result is displayed in Fig. 3.7a as a function of dimensionless time γt for $\Omega/\gamma = 0.5$. The distribution is visualized for ten different values of n, i.e. the number of electrons that have been transported to the right reservoir. It is evident that zero electrons ($n = 0$) have been transported initially in accordance with the initial condition, see Sec. 2.4.1.

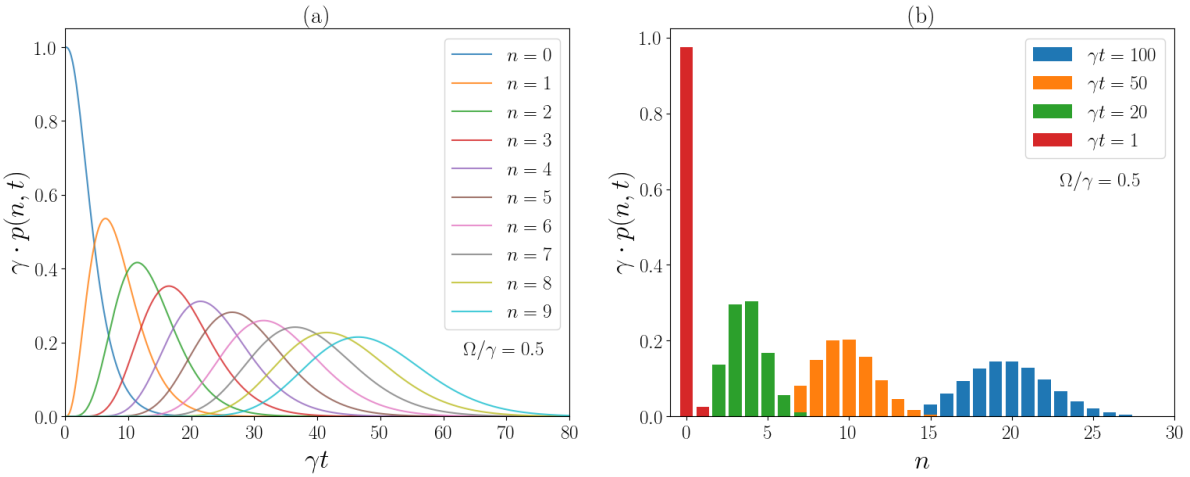

Figure 3.7: *(a) The numerically calculated probability distribution $p(n,t)$ as a function of dimensionless time γt. The distribution is visualized for ten different values of n, i.e. the number of electrons that have been transferred to the right reservoir. (b) The same distribution as in (a), but here displayed as a function of n at four different times γt. $\Omega/\gamma = 0.5$ and the initial condition $g(\chi, 0) = (1, 0, 0)$ have been used for both figures.*

It is also clear that the probability distribution for $n = 0$ goes to zero as time increases, and this is expected since the demon only is transporting electrons towards the right reservoir.

When looking at $n > 0$, we see that the maximum position of $p(n,t)$ is shifted towards larger times. Furthermore, the width of the distribution increases as time proceeds. In Fig. 3.7b, $p(n,t)$ is visualized as a function of n at four different times, also for $\Omega/\gamma = 0.5$. The distribution clearly moves along the n-axis as time is increased. It can be noted that the probability distribution is more narrow for smaller values of γt, and as larger γt are studied, the distribution gets broader.

Figures 3.7a and 3.7b show similar behaviour, a narrow distribution at small γt that gets broader as γt is increased. The narrow shape for small γt can be understood by considering the initial condition. At $\gamma t = 0$, no electrons have been transferred to the right reservoir, and n is therefore well-known. As a result, the distribution becomes narrow at small γt since the uncertainty in n is small. As γt increases, however, the uncertainty in n increases, and a broader distribution is observed. Furthermore, as larger n are studied, the distribution is centered around larger and larger values of γt. Since electrons only are transported towards the right reservoir, the probability distribution of having, for example, $n = 2$ is centered at a earlier time than the probability distribution for $n = 7$.

Appendix C contains a validity check of the probability distribution in Fig. 3.7. The validity check shows the normalization of $p(n,t)$.

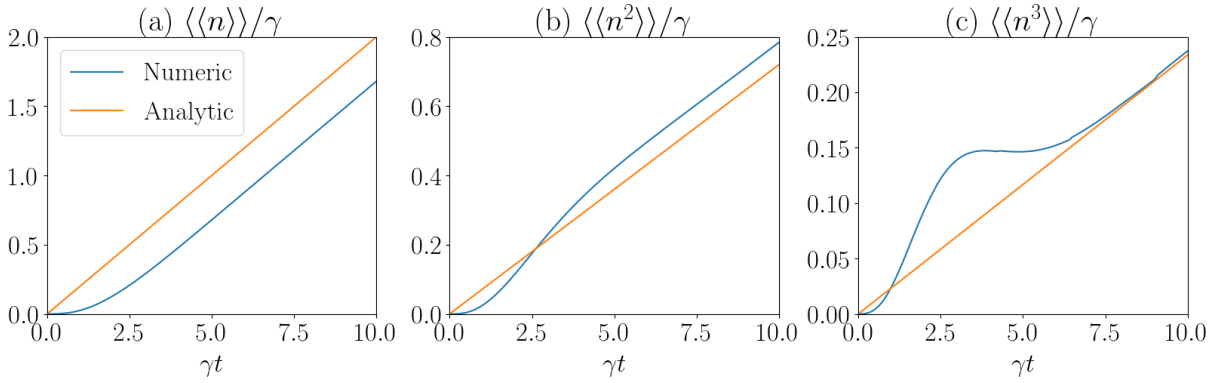

Figure 3.8: *The first three cumulants of $p(n,t)$ calculated for $\Omega/\gamma = 0.5$. Here, all cumulants are normalized by γ. The numerical (blue line) and analytical (orange line) results are compared in the graphs. (a) The first normalized cumulant, $\langle\langle n\rangle\rangle/\gamma$. (b) The second normalized cumulant, $\langle\langle n^2\rangle\rangle/\gamma$. (c) The third normalized cumulant, $\langle\langle n^3\rangle\rangle/\gamma$. All cumulants are displayed as functions of dimensionless time γt.*

The first three cumulants of the probability distribution in Fig. 3.7 are presented as the blue, solid lines in Fig. 3.8, while the orange, solid lines are the analytical cumulants given by Eqs. (3.19)-(3.21). All cumulants are here normalized by γ, and displayed as functions of dimensionless time γt, for $\Omega/\gamma = 0.5$. For all three graphs, it can be seen that the numerical cumulants account for both the short and long time behaviour of the complete system. Here, the short time behaviour is the dynamics of the complete system before steady state is reached. The analytical cumulants, however, only account for the long time behaviour. Clearly, the numerics become linear as steady state is reached, and this is expected since the long time cumulants are linear in time for any system, see Eq. (2.25). It should be noted that there is a discrepancy between the numerics and the analytics in all three plots. The discrepancy can be understood by considering the cumulant generating function in the long time limit given by Eq. (2.23). This function is, as discussed in Sec. 2.4, determined up to a small correction, and this correction is

the origin of the discrepancy. From Fig. 3.8a it is evident that the mean number of electrons that have been transferred to the right reservoir is increasing with time. This agrees with the implementation of the demon; it only transports electrons towards the right reservoir, and hence, the mean should increase with time. As seen in Fig. 3.8b, the second cumulant is also increasing with time, this is in accordance with the observations of Fig. 3.7 where the width of the probability distribution clearly increases with time. The third cumulant describes the skewness of the distribution. In this study, a positive, and increasing skewness is observed for all times as can be seen in Fig. 3.8c. The increase in skewness is, however, not clearly visible in Fig. 3.7.

3.3 Monte Carlo simulation

This section is devoted to the results generated by the Monte Carlo simulation discussed in Sec. 2.5. A comparison of the Monte Carlo simulation and the analytical and numerical FCS is also presented.

Figure 3.9 displays a possible time trace of the state of the double quantum dot system that can be recorded in a measurement; this time trace was generated by the Monte Carlo simulation. Each time the system returns to $|00\rangle$, one electron has been transported to the right reservoir. Hence, by counting the number of times the system returns to $|00\rangle$, we can keep track of the number of transferred electrons. For the time trace displayed in Fig. 3.9, five electrons have been transferred after 0.05 s.

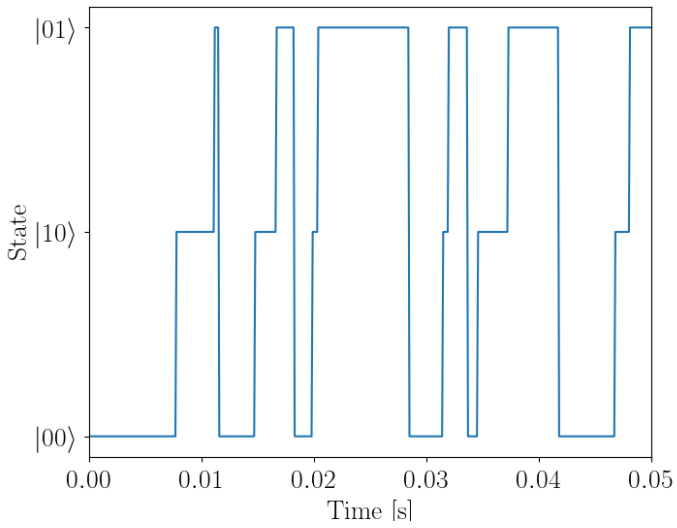

Figure 3.9: *The graph shows a possible time trace of how the state of the double QD system evolves in time. The trace was generated in a Monte Carlo simulation. Here, the tunneling rates are chosen as* $\Gamma_L = \Gamma_R = \gamma = 1000\ s^{-1}$*, the temperature is* $T = 0.1\ K$*, and the voltage bias is* $V = -24.0\ \mu V$*, and the chemical potentials are symmetric around* $\epsilon_0 = 0$*,* $\mu_L = eV/2$ *and* $\mu_R = -eV/2$*.*

By performing a large number of simulations, and recording how many electrons, n, that have been transferred to the right reservoir at each discrete time in every simulation, the first central moment can be calculated via $\mu = \langle n \rangle$, where $\langle \ldots \rangle$ denotes the sample

mean. This corresponds to the first cumulant of the probability distribution $p(n,t)$ discussed in Sec. 2.4. The second and third cumulants are given by the second and third central moments, and are calculated using $\mu_i = \langle (n - \langle n \rangle)^i \rangle$, $i = 2, 3$.

In Figs. 3.10 and 3.11, the cumulants calculated from the Monte Carlo simulations are displayed together with the cumulants obtained from the full counting statistics. The system parameters are chosen differently for the various figures as specified in the corresponding captions. For the first order cumulants in Figs. 3.10a and 3.11a, there is good agreement between the numerical FCS and the Monte Carlo simulations. It can be noted that both these methods account for small times as well as long times. As steady state is reached, both the numerical FCS and the Monte Carlo simulations have the same slope as the analytical cumulants.

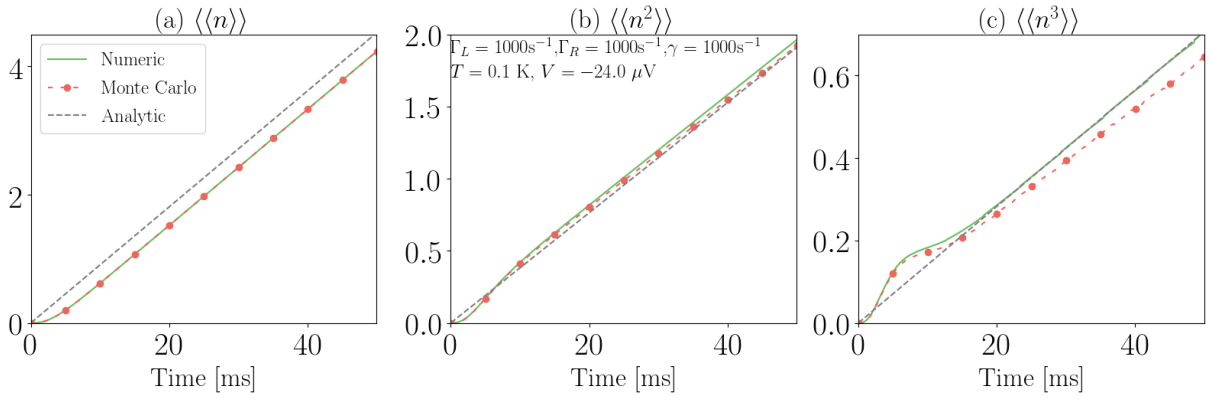

Figure 3.10: *The first three cumulants when using the following system parameters:* $\Gamma_L = \Gamma_R = \gamma = 1000\ s^{-1}$*;* $T = 0.1\ K$*;* $V = -24.0\ \mu V$*; and a voltage bias symmetric around* $\epsilon_0 = 0$*, i.e.* $\mu_L = \epsilon_0 + eV/2$ *and* $\mu_R = \epsilon_0 - eV/2$*. The green, solid lines correspond to the numerical cumulants generated by the FCS; the gray, dashed lines are the analytical cumulants from the FCS; and the red, dashed and dotted lines are the cumulants calculated with data from 1 000 000 Monte Carlo simulations. (a) First cumulant, (b) second cumulant, (c) third cumulant.*

For the second and third order cumulants, the Monte Carlo simulation deviates from the FCS. This is probably due to the number of performed Monte Carlo simulations; if a larger number of simulations had been performed, the agreement would have been enhanced. Higher order cumulants describe the behaviour of the tails of a probability distribution. When drawing random numbers, as done in the Monte Carlo simulations, it is most probable to draw numbers close to the mean value; it will be rare to draw numbers close to the tails. Hence, to calculate higher order cumulants, a large number of simulations is required to get good precision. For the data presented here, 1 million simulations were run, and we clearly see that this number must be increased to get better agreements for the second and third cumulants. As a conclusion, to measure the higher order cumulants in a real experiment, a large number of recordings of the system dynamics is required. Here we see, under ideal conditions, that 1 million recordings are not enough to get good precision.

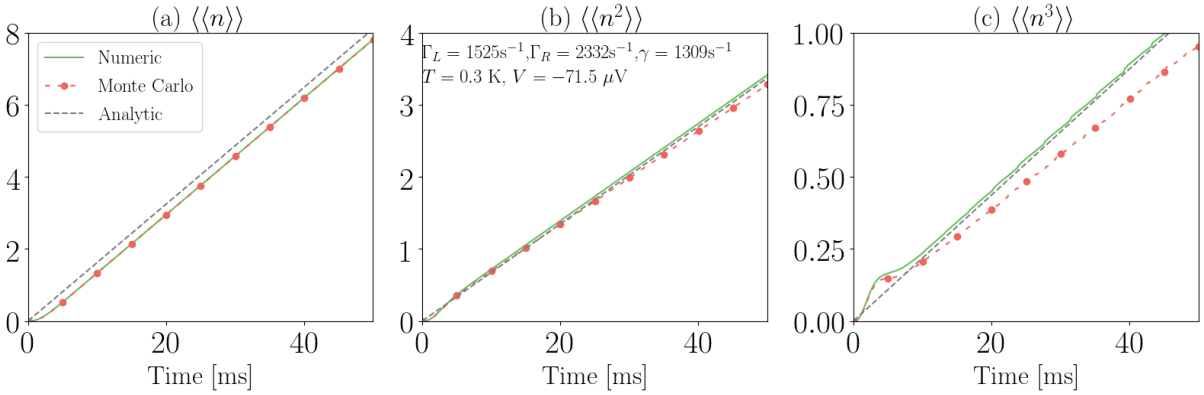

Figure 3.11: *The first three cumulants when using the following system parameters:* $\Gamma_L = 1525\ s^{-1}$, $\Gamma_R = 2332\ s^{-1}$, $\gamma = 1309\ s^{-1}$; $T = 0.3\ K$; $V = -71.5\ \mu V$; *and a voltage bias symmetric around* $\epsilon_0 = 0$, *i.e.* $\mu_L = eV/2$ *and* $\mu_R = -eV/2$. *The green, solid lines correspond to the numerical cumulants generated by the FCS; the gray, dashed lines are the analytical cumulants from the FCS; and the red, dashed and dotted lines are the cumulants calculated with data from 1 000 000 Monte Carlo simulations. (a) First cumulant, (b) second cumulant, (c) third cumulant.*

It should be noted that it appears as if the numerics and analytics in Figs. 3.10 and 3.11 overlap for the second and third cumulants, but this is not the case. The discrepancy that is visible in Fig. 3.8 is still present, but not as clearly visible. We can also note that the system reaches steady state faster when the tunneling rates are increased.

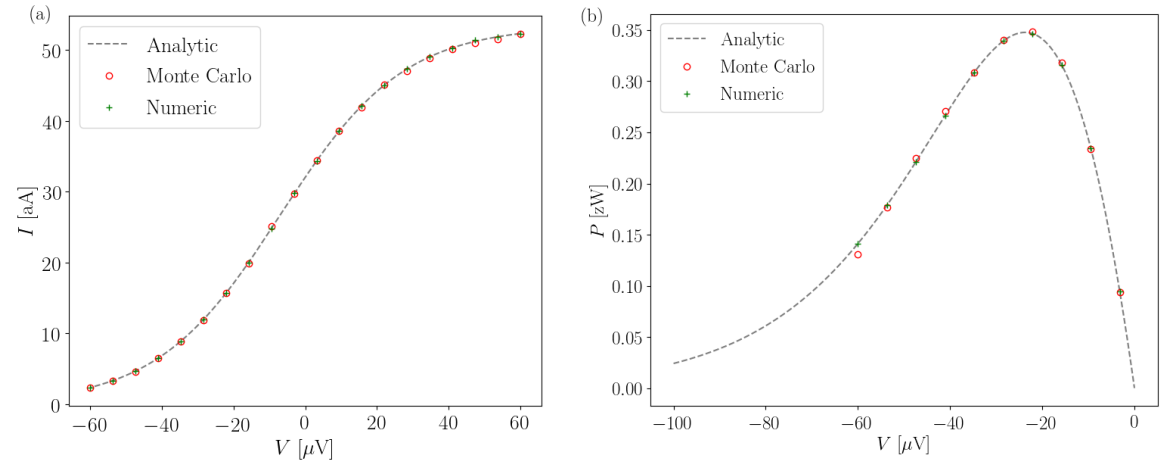

Figure 3.12: *(a) Steady state current as a function of voltage bias* V, *here calculated for* $\Gamma_L = \Gamma_R = \gamma = 1000\ s^{-1}$, $T = 0.1\ K$, *and the chemical potentials* $\mu_L = eV/2$ *and* $\mu_R = -eV/2$, *with* $\epsilon_0 = 0$. *The dashed, gray line is calculated with Eq. (3.6); the red circles are calculated with the Monte Carlo simulation; and the green plus-signs are calculated with the numerical FCS. (b) The electrical power of the current displayed in Fig. 3.12a.*

Figure 3.12a displays the steady state current in the double QD system as a function of voltage bias V for the case when $\Gamma_L = \Gamma_R = \gamma = 1000\ \text{s}^{-1}$, $T = 0.1$ K, and $\mu_L = eV/2$ and $\mu_R = -eV/2$, with $\epsilon_0 = 0$. Three cases are presented in the figure, one where the current is calculated with Eq. (3.6), one where the current is calculated with the Monte Carlo simulation, and one where the numerical FCS has been used. The current obtained

with the Monte Carlo method was calculated with the first cumulant from Fig. 3.10a for $t \to \infty$ according to $I = e\partial_t \langle\langle n(t \to \infty)\rangle\rangle$. Clearly, the three methods agree, and the current is in the order of tens of atto-Amperes. Figure 3.12b shows the electrical power of the current in Fig. 3.12a as a function of negative voltage bias. The power is in the order of one-tenth of a zepto-Watt.

Chapter 4

Conclusions

This thesis has examined the transport properties and the full counting statistics of electrons in a double quantum dot system that is operated by a Maxwell demon. Our results clearly show that the implementation of the demon works in theory. To examine the transport properties, rate equations and full counting statistics were used. These two approaches yield the same analytical expressions for the electrical current through the quantum dots as well as the electrical power. We see that the demon is transporting electrons, without performing any net work on them, against voltage biases in the order of tens of micro-Volts when the temperature of the complete system and the electron tunneling rates are in the order of hundreds of milli-Kelvins and thousands of events per second, respectively. These parameters are typical for systems similar to the one studied in this thesis [27]. The currents in this regime are in the order of tens of atto-Amperes, and the electrical power gained is in the order of one-tenth of a zepto-Watt. Experimentally, it is fully possible to measure currents that are in the order of atto-Amperes, this is done by counting the passage of individual electrons [27]; and this suggests that an experimental realization of the system is possible.

In addition, full counting statistics gives the cumulants of the probability distribution describing the number of electrons transferred through the system at a given time. These cumulants have been calculated both analytically and numerically, and the results agree in the long time limit due to the analytics only being valid in that regime. The statistical nature of the probability distribution was mapped out for some different limits of the transition rates. When one or two of the transition rates is much larger than the others, the system follows Poissonian statistics. Furthermore, for equal transition rates, we obtained an analytical expression for the probability distribution in the long time limit, and this distribution is related to the Poisson distribution. Finally, the probability distribution was also evaluated numerically, but for non-equal transition rates.

Furthermore, the dynamics of the system was simulated with a Monte Carlo method for specific system parameters. The first order cumulants generated with this Monte Carlo method agree well with the full counting statistics, but higher order cumulants leave a lot to be desired. The poor agreement for higher order cumulants is most probably due to the number of simulations. The agreement is believed to improve with an increased amount of simulations. The convergence of the Monte Carlo cumulants as a function of the number of simulations could in the future be studied.

The implementation of Maxwell's demon presented in this thesis is based on the assumption that the double quantum dot system can be operated infinitely fast, and that the demon can measure the occupation of the quantum dots error-free and without delay.

An experimental realization must therefore make sure that the feedback from the demon is faster than the electron tunneling rates so that the energy levels of the quantum dots can be moved up or down before unwanted tunneling events occur. In addition, the speed at which the energy levels are moved plays a crucial role, it must also be faster than the tunneling rates to avoid unwanted tunneling events. Furthermore, measurement errors should be minimized in order to maximize the performance of the demon; the transition rates should, in an experiment, be tuned to be smaller than the detection rate. Then the risk of missing tunneling events is reduced.

Finally, as the electrons are transferred against the voltage bias, we see that heat from the electron reservoirs is converted into useful work resulting in a cooling of the reservoirs. Papers examining similar systems argue that an application of Maxwell's demon could be to cool down gases [1, 9], [2, 8]. We further suggest that it should be investigated whether the output power can be used to power for example heat engines on the nano-scale. It should, however, be stressed that the work made here is mainly concentrating on the investigation whether it is feasible to implement a Maxwell demon in a double quantum dot system that could be used to study information-to-energy conversion.

Chapter 5

Outlook

The study made in this thesis stands as a starting point for further studies on the Maxwell demon in the double quantum dot system. In future studies, the demon can be implemented in the model as a detector measuring the state of the quantum dots. The detector could be realized by using a single electron transistor (SET), that is a quantum dot coupled to two leads. The SET is coupled, by Coulomb interaction, to the left and right quantum dots asymmetrically. The current through the SET is affected by the state of the double quantum dots, and is decreased when either of the dots is occupied. By using the asymmetrical coupling, the amplitude of the current decrease is dependent on whether the left or the right dot is occupied, and in this way, the transport of individual electrons can be studied.

To experimentally realize the system, the setup visualized in Fig. 2.2 would be the starting point. To this layout, a detector must be added, and two possible choices would be either a SET, as discussed above, or a quantum point contact (QPC). A SET detector has already been used in a similar system realizing Szilard's engine with a single electron [8]. On the other hand has a QPC been used in a double quantum dot system very similar to the one discussed here to detect single electrons [28]. Both [8] and [28] indicate that the system studied in this thesis is feasible to construct with a detector able to measure the passage of single electrons. However, to be able to resolve fast system dynamics, the detection rate should be faster than the fastest transition rate in the system. Another challenge of an experimental realization would be to implement the cycle in Fig. 2.5; it is important that the work related to lifting and lowering the energy levels sum up to zero so that no net work has been put into the system. An experimental suggestion of a similar scheme can be found in [6].

The theoretical work, on the other side, could involve an extension of the Monte Carlo method where a more realistic detector model is implemented. At the present moment, the state of the double quantum dots is assumed to be measured perfectly, and without errors and delay. An extension could include realistic detector noise, and error-detection. In this way, the simulations would be more comparable to real experiments. Such simulations could be useful when designing experimental realizations of the system, and when determining the number of measurements required for obtaining good statistics. In the end, a more realistic Monte Carlo method could be a helpful tool for pointing experimental work in the right directions.

Another interesting aspect of introducing the demon as a detector is that the role of information can be studied. The information gathered by the detector should be used in a feedback loop to operate the quantum dots, which opens up the possibility to study

information-to-energy conversion, and to verify whether the total entropy production in the complete system is positive. A validity check of an implemented feedback loop could be done by studying Jarzynski's generalized equality for systems with feedback control, and an investigation whether it is possible to derive a maximum efficiency for the system could be carried out.

To this point, coherence between the quantum dots has been out of the picture. The present model could be extended to a quantum version where coherent states are present in the system. A natural question that arises is how Maxwell's demon is implemented in such a system.

As a last comment, the results from this thesis will, in the future, be published in a peer reviewed journal.

Appendix A

Derivation of probability distribution - simple case

With the saddle point approximation method, the probability distribution, given by Eq. (2.24), can be written as

$$p(n,t) \approx \frac{1}{\sqrt{2\pi f''(\chi^*)}} e^{-f(\chi^*)}, \tag{A.1}$$

where $f(\chi) = in\chi - \lambda(\chi)t$, with $\lambda(\chi)$ being the eigenvalue given by Eq. (3.10) for $l = 0$ when $\gamma = \gamma_L = \gamma_R$, and χ^* is the number that solves the equation $f'(\chi) = 0$. The derivative of $f(\chi)$ is $f'(\chi) = in - \lambda'(\chi)t$, and this gives that $\chi^* = -3i\ln(3n/\gamma t)$. Furthermore, $f''(\chi) = -\lambda''(\chi)t$, and plugging this and the information given above into Eq. (A.1), the following distribution is obtained,

$$p(n,t)_{\gamma=\gamma_L=\gamma_R} \approx \sqrt{\frac{3}{2\pi n}} \left(\frac{\gamma t e}{3n}\right)^{3n} e^{-\gamma t}. \tag{A.2}$$

The normalization of this distribution is displayed in Fig. A.1 as a function of dimensionless time γt.

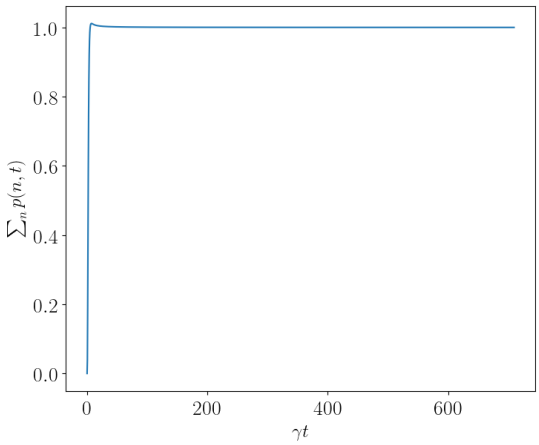

Figure A.1: *Normalization of the distribution given in Eq. (A.2) as a function of dimensionless time γt.*

Appendix B

Analytical expression for the fourth cumulant

The analytical expressions for the first to third order cumulants are given in Eqs. (3.19)-(3.21) in Sec. 3.2.2. The fourth cumulant is given below.

$$\langle\langle n^4\rangle\rangle = \frac{\gamma\gamma_L\gamma_R - 36\left(\frac{d\lambda_1}{d\chi}\Big|_{\chi=0}\right)^2 \frac{d^2\lambda_1}{d\chi^2}\Big|_{\chi=0} - 2(\gamma+\gamma_L+\gamma_R)\left[3\left(\frac{d^2\lambda_1}{d\chi^2}\Big|_{\chi=0}\right)^2 + 4\frac{d\lambda_1}{d\chi}\Big|_{\chi=0}\frac{d^3\lambda_1}{d\chi^3}\Big|_{\chi=0}\right]}{\gamma\gamma_L+\gamma\gamma_R+\gamma_L\gamma_R} t. \tag{B.1}$$

The second and third derivatives in the fourth cumulant are obtained in the same way as the first derivative in Eq. (3.18) was obtained.

Appendix C

Validity check of full counting statistics

Figure C.1 displays the normalization of $p(n,t)$ as a function of time. This acts as a validity check of the results presented in Fig. 3.7. The normalization clearly is 1 for all times, $p(n,t)$ is indeed a probability distribution.

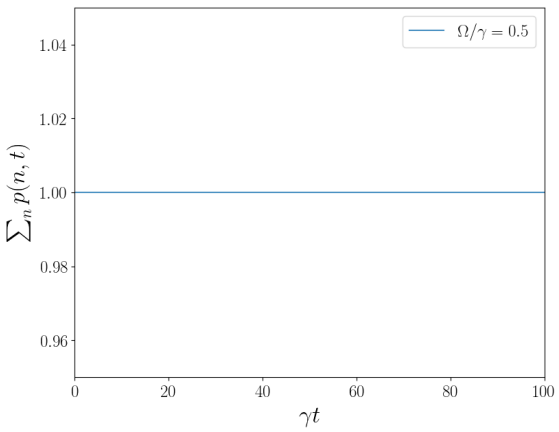

Figure C.1: *Validity check of the probability distribution displayed in Fig. 3.7. The distribution is summed over the variable n, that is the number of electrons that have been transferred to the right reservoir, and the distribution is clearly normalized over time. Here, $\Omega/\gamma = 0.5$.*

Appendix D

Second and third cumulants of the electrical power

Figures D.1-D.3 display the second and third order cumulants for some different choices of the normalized tunneling rates Γ_L/γ and Γ_R/γ.

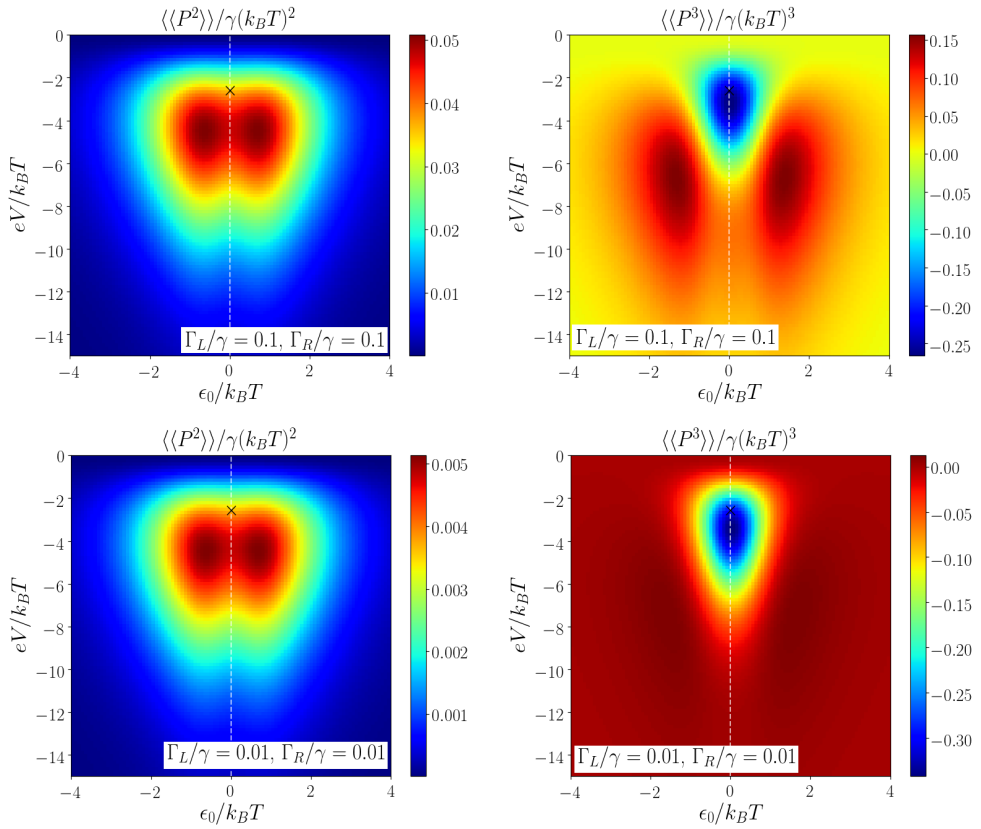

Figure D.1: *Second and third cumulants of the electrical power as functions of* ϵ_0/k_BT *and* eV/k_BT*, here plotted for equal, but small tunneling rates* Γ_L/γ *and* Γ_R/γ*. The chemical potentials are* $\mu_L = eV/2$ *and* $\mu_R = -eV/2$*.*

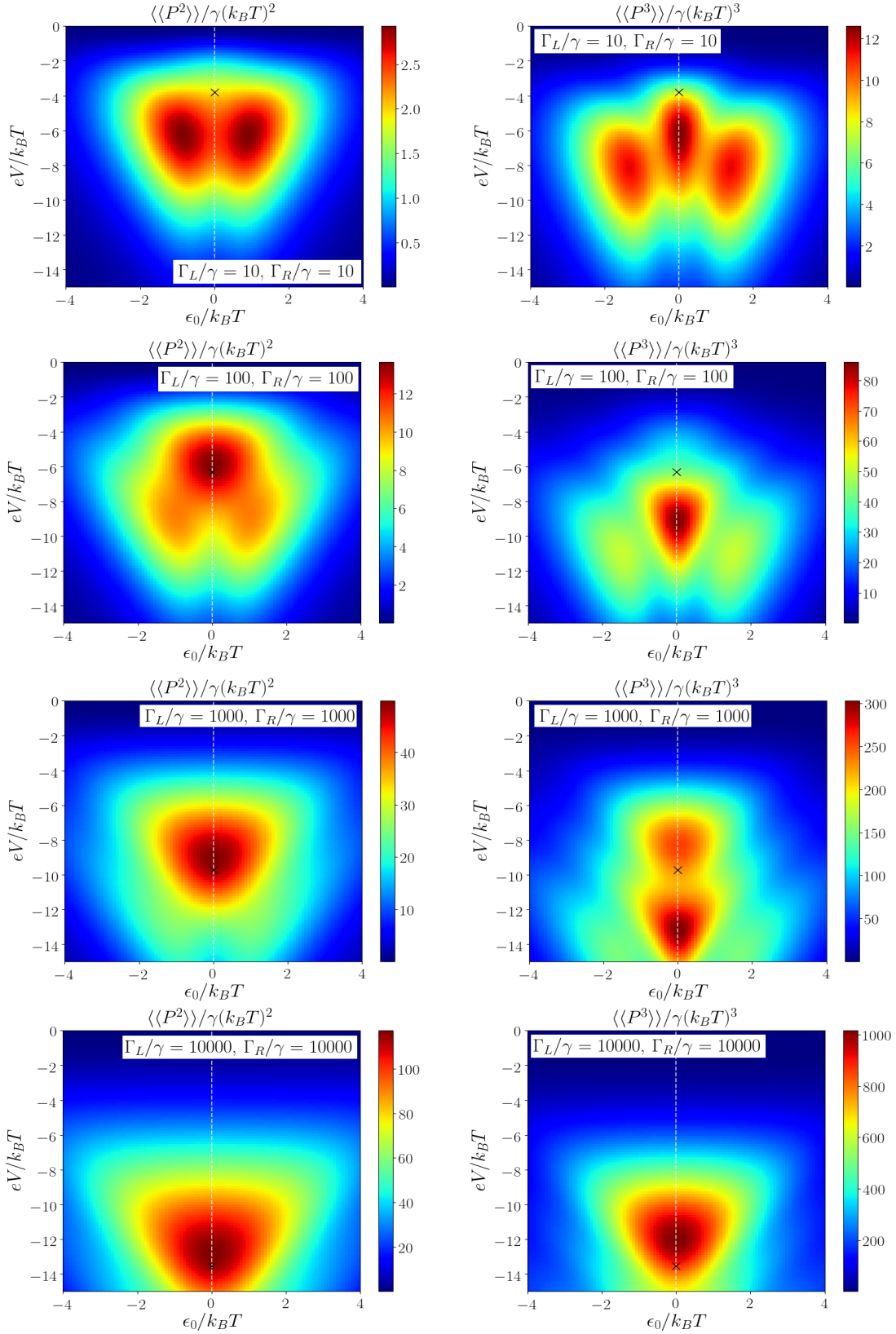

Figure D.2: *Second and third cumulants of the electrical power as functions of* ϵ_0/k_BT *and* eV/k_BT*, here plotted for equal, but increasing tunneling rates* Γ_L/γ *and* Γ_R/γ*. The chemical potentials are* $\mu_L = eV/2$ *and* $\mu_R = -eV/2$*.*

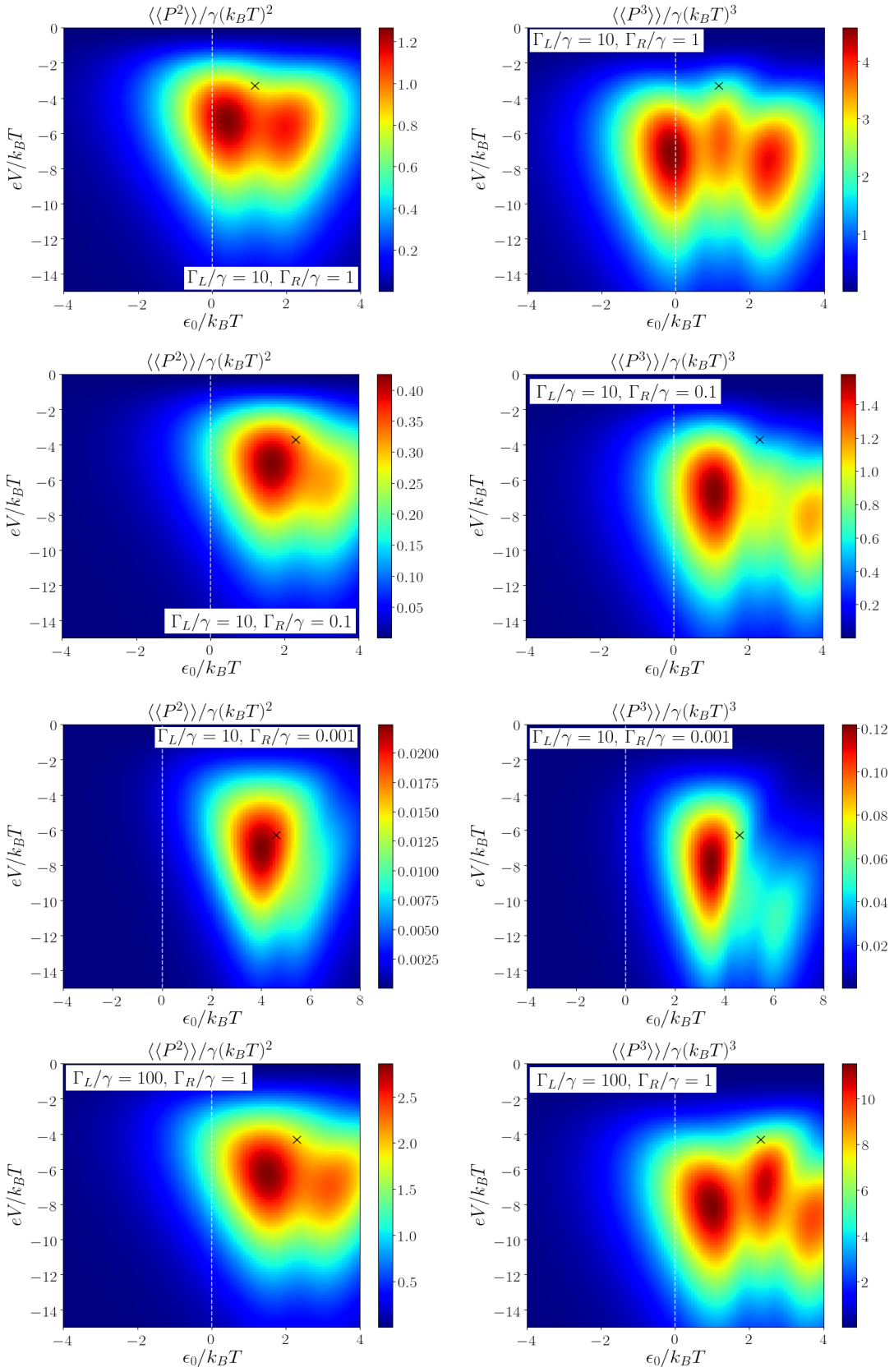

Figure D.3: *Second and third cumulants of the electrical power as functions of ϵ_0/k_BT and eV/k_BT, here plotted for non-equal tunneling rates Γ_L/γ and Γ_R/γ. The chemical potentials are $\mu_L = eV/2$ and $\mu_R = -eV/2$.*

References

[1] S. Vinjanampathy, J. Anders. *Quantum thermodynamics.* Contemporary Physics, vol. 57, p. 545-579, 2016.

[2] J. Pekola. *Towards quantum thermodynamics in electronic circuits.* Nature physics, vol. 11, p. 118-123, 2015.

[3] R. Landauer. *Irreversibility and heat generation in the computing process.* IBM J. Res. Develop., vol. 5, 1961.

[4] C.H. Bennett. *The thermodynamics of computation - a review.* International Journal of Theoretical Physics, vol. 21, p. 905-940, 1982.

[5] P. Strasberg, G. Schaller, T. Brandes, M. Esposito. *Thermodynamics of a Physical Model Implementing a Maxwell Demon.* Physical Review Letters, vol. 110, p. 04060(1)-040601(5), 2013.

[6] D. Averin, M. Möttönen, J. Pekola. *Maxwell's demon based on a single-electron pump.* Physical Review B, vol. 84, p. 245448(1)-245488(5), 2011.

[7] S. Toyabe, T. Sagawa, M. Ueda, E. Muneyuki, M. Sano. *Experimental demonstration of information-to-energy conversion and validation of the generalized Jarzynski equality.* Nature physics, vol. 6, p. 988-992, 2010.

[8] J. Koski, V. Maisi, J. Pekola, D. Averin. *Experimental realization of a Szilard engine with a single electron.* Proc. Natl Acad. Sci. USA, vol. 111, p. 13786-13789, 2014.

[9] M. Raizen. *Demon entropy and the quest for absolute zero.* Scientific American, vol. 304, p. 54-59, 2011.

[10] Y. Blanter, M. Büttiker. *Shot noise in mesoscopic conductors.* Physics Reports, vol. 336, p. 1-166, 2000.

[11] R. de Picciotto et al. *Direct observation of a fractional charge.* Nature, vol. 389, p. 162-164, 1997.

[12] L. Saminadayar, D. Glattli. *Observation of the e/3 Fractionally Charged Laughlin Quasiparticle.* Physical Review Letters, vol. 79, p. 2526-2529, 1997.

[13] X. Jehl, M. Sanquer, R. Calemczuk, D. Mailly. *Detection of doubled shot noise in short normal-metal/superconductor junctions.* Nature, vol. 405, p. 50-53, 2000.

[14] A. Kozhevnikov, R. Schoelkopf, D. Prober. *Observation of Photon-Assisted Noise in a Diffusive Normal Metal-Superconductor Junction.* Physical Review Letters, vol. 84, p. 3398-3401, 2000.

[15] A. Fuhrer, et al. *Few Electron Double Quantum Dots in InAs/InP Nanowire Heterostructures.* Nano Letters, vol. 7, p. 243-246, 2007.

[16] M. Nilsson, et al. *Single-electron transport in InAs nanowire quantum dots formed by crystal phase engineering.* Physical Review B, vol. 93, p. 195422(1)-195422(7), 2016.

[17] C.G. Knott. *Life and scientific work of Peter Guthrie Tait.* London: Cambridge University Press, p. 213-215, 1911.

[18] K. Maruyama, F. Nori, V. Vedral. *The physics of Maxwell's demon and information.* Reviews of Modern Physics, vol. 81, p. 1-23, 2009.

[19] H. Bruus, K. Flensberg. *Many-Body Quantum Theory in Condensed Matter Physics - An introduction.* New York: Oxford University Press Inc., 2004.

[20] L. Levitov, H. Lee, G. Lesovik. *Electron counting statistics and coherent states of electric current.* Journal of Mathematical Physics, vol. 37, p. 4845-4866, 1996.

[21] C. Flindt, T. Novotny, A.P. Jauho. *Full counting statistics of nano-electromechanical systems.* Europhysics Letters, vol. 69, p. 475–481, 2005.

[22] G. Schaller. *Open Quantum Systems Far from Equilibrium.* Springer, 2014.

[23] A. Jordan, E. Sukhorukov. *Transport Statistics of Bistable Systems.* Physical Review Letters, vol. 93, p. 260604(1)-260604(4), 2004.

[24] G. Schaller, G. Kießlich, T. Brandes. *Counting statistics in multistable systems.* Physical Review B, vol. 81, p. 205305(1)-205305(5), 2010.

[25] J. Schnakenberg. *Network theory of microscopic and macroscopic behavior of master equation system.* Review of Modern Physics, vol. 48, p. 571-585, 1976.

[26] P. Potts. *Stochastic analysis of unidirectional transitions on a ring.* Private communication, June 2018.

[27] S. Gustavsson, et al. *Counting statistics of Single Electron Transport in a Quantum Dot.* Physical Review Letters, vol. 96, p. 076605(1)-076605(4), 2006.

[28] B. Küng, et al. *Irreversibility on the Level of Single-Electron Tunneling.* Physical Review X, vol. 2, 2012.